The role of the flanking polyQ regions of Huntingtin exon 1 on lipid binding: Insights into Huntington's disease

Gonçalo Filipe Ferreira Damas

Thesis to obtain the Master of Science Degree in

Biotechnology

Supervisors

Dr. Ana Margarida Pereira de Melo

Prof. Ana Margarida Nunes da Mata Pires de Azevedo

Examination Committee

Chairperson: Prof. Miguel Nobre Parreira Cacho Teixeira

Supervisor: Dr. Ana Margarida Pereira de Melo

Members of the Committee: Prof. Fábio Monteiro Fernandes

May 2023

Preface

The work presented in this thesis was performed at the Institute for Bioengineering and Biosciences of Instituto superior Técnico (Lisbon, Portugal), during the period March – September 2022, under the supervision of Dr. Ana Melo and Prof. Ana Azevedo.

Declaração

Declaro que o presente documento é um trabalho original da minha autoria e que cumpre todos os requisitos do Código de Conduta e Boas Práticas da Universidade de Lisboa.

Declaration

I declare that this document is an original work of my own authorship and that it fulfills all the requirements of the Code of Conduct and Good Practices of the Universidade de Lisboa.

Agradecimentos

Antes de mais, quero agradecer à Doutora Ana Melo e Professora Ana Azevedo por me terem aceitado nos seus laboratórios e por partilharem todos os seus conhecimentos comigo, pela boa disposição e pela sempre presente vontade de ajudar. Ao Professor Pietro pelos conhecimentos partilhados sobre fluorescência. Ao Aleksander Fedorov pela adquisição dos dados experimentais de fluorescência resolvida no tempo. A todas as restantes pessoas no laboratório pela sua boa disposição, companhia e ajuda. À Lise, à Linda e ao Tomás que já me aturam há seis anos. Ao Vital com quem partilhei o teto durante dois anos. Aos meus pais e à minha família (em especial à minha Avó Ana que não teve a oportunidade de me ver acabar o mestrado) por todo o seu apoio e amor incondicional. A todos os outros amigos, professores e conhecidos que me ajudaram a melhorar e a tornar na pessoa que sou hoje.

Agradeço também à Fundação para a Ciência e Tecnologia peço financiamento do projeto “The aggregation-prone structures of Huntingtin exon 1 at the single-molecule level: Influence of membranes and implications in Huntington disease” (PTDC/BIA-BFS/30959/2017).

Resumo

A doença de Huntington (HD) é uma desordem neurodegenerativa grave, autossómica dominante e progressiva. A HD é causada por uma expansão de poliglutaminas (poliQ) no primeiro exão da proteína huntingtina (HTT). O fragmento HTT do exão 1 (Httex1) com uma expansão de poliQ é altamente tóxico e forma agregados/corpos de inclusão em células neurais, replicando grande parte da patologia da HD. As membranas biológicas desempenham um papel crítico na agregação e toxicidade do Httex1. Neste trabalho, a interação do Httex1-23Q com vesículas unilamelares grandes (LUVs) de diferentes composições lipídicas (com lípidos zwitteriónicos, misturas de “rafts” lipídicas e lípidos aniónicos) foi analisada por fluorescência do Acrylodan e Atto 488. Cada região adjacente ao domínio poliQ – N-terminal Nt17 e C-terminal região rica em prolinas (PPR) – foi marcada de forma específica com fluoróforos reativos a tiol. Os resultados com Acrylodan mostram que o Httex1 se liga de forma similar a vesículas lipídicas zwitteriónicas e misturas de “rafts” lipídicas (componente hidrofóbico). Além disso, o segmento N-terminal Nt17 interage com as membranas lipídicas e o C-terminal PRR permanece exposto ao solvente no estado ligado à membrana. Finalmente, os decaimentos de anisotropia de fluorescência do Atto 488 ligado ao Nt17 ou ao PRR também revelam que estes domínios experimentam dinâmicas diferentes após a ligação à membrana. O PRR é altamente flexível (semelhante a uma proteína intrinsecamente desordenada) e o Nt17 adota um estado menos flexível ao ligar-se a membranas lipídicas aniónicas.

Palavras-chave: Doença de Huntington; Exão-1 da huntingtina; Membranas Lipídicas; Espectroscopia de Fluorescência

Abstract

Huntington's disease (HD) is a severe, autosomal dominant and progressive neurodegenerative disorder. HD is caused by a polyglutamine (polyQ) expansion within the first exon of the huntingtin (HTT) protein. The HTT exon 1 (Httex1) fragment with a polyQ expansion is highly toxic and forms aggregates/inclusion bodies in neural cells, replicating much of HD's pathology. Biological membranes play a critical role in Httex1 aggregation and toxicity. In this work, the interaction of Httex1-23Q with large unilamellar vesicles (LUVs) of different lipid compositions (with pure zwitterionic lipids, raft-mimicking mixtures, and anionic lipids) was analyzed by Acrylodan and Atto 488 fluorescence. Each flanking polyQ region – N-terminal Nt17 and C-terminal proline-rich region (PPR) – was site-specifically labeled with these thiol-reactive fluorophores. The Acrylodan results show that the Httex1 binds in a similar extension to zwitterionic and raft-mimicking lipid vesicles (hydrophobic component). Moreover, the N-terminal Nt17 segment interfaces lipid membranes and the C-terminal PRR remains solvent exposed in the membrane-bound state. Finally, fluorescence anisotropy decays of Atto 488 attached to Nt17 or PRR also reveal that these domains experience different dynamics upon membrane-binding. The PRR is highly flexible (as an IDP) and the Nt17 adopts a less flexible state upon binding to anionic lipid membranes.

Keywords: Huntington's disease; Huntingtin exon 1; Lipid Membranes; Fluorescence Spectroscopy

Table of Contents

List of Figures

List of Tables

List of Abbreviations

Acrylodan	6-acryloyl-2-dimethylaminonaphthalene
AFM	atomic force microscopy
Alexa 488	Alexa Fluor™ 488 C_5 maleimide
Alexa 594	Alexa Fluor™ 594 C_5 maleimide
APDs	avalanche photodiode detectors
Atto 488	Atto 488 maleimide
Buffer A	50 mM Tris-HCl, pH 8.0, 500 mM NaCl, 15 mM Imidazole
Buffer B	50 mM Tris-HCl, pH 8.0, 500 mM NaCl, 500 mM Imidazole
Buffer C	50 mM Tris-HCl, pH 8.0, 150 mM NaCl, 15 mM Imidazole
Buffer SEC	50 mM Tris-HCl, pH 8.0, 200 mM NaCl
Chol	cholesterol
CNS	central nervous system
cpm	counts per molecule
Cryo-EM	cryo-electron microscopy
CV	column volumes
DTT	dithiothreitol
ER	endoplasmic reticulum
ET_{eff}	efficiency of transfer
FCS	fluorescence correlation spectroscopy
FRET	Förster resonance energy transfer
HAP40	HTT-associated protein 40
His_6-Ulp1	His_6-Ubiquitin-like-specific protease 1
HTT	huntingtin
Httex1	huntingtin exon 1
IMAC	Immobilized Metal Affinity Chromatography
IPTG	isopropyl ß-D-1-thiogalactopyranoside
Km	kanamycin
Labeling buffer	20 mM Tris, pH 7.4, 50 mM NaCl, 6 M guanidine hydrochloride
LB	Luria Broth
Loading buffer	50 mM Tris-HCl, pH 6.8, 100 mM DTT, 2% SDS, 0.1% bromophenol blue, 10% glycerol
LUVs	large unilamellar vesicles
MLVs	multilamellar vesicles
mHTT	mutant huntingtin
MW	molecular weight
N	number of molecules
NA	numerical aperture
NES	nuclear export signal
Nt17	N-terminal 17 amino acid
OD_{600}	optical density at 600 nm
Oligo hybridization buffer	10 mM Tris-HCl, pH 8, 15 mM $MgCl_2$, 100 mM NaCl
PMSF	phenylmethylsulphonyl fluoride
polyQ	polyglutamine

POPC	1-palmitoyl-2-oleoyl-*sn*-glycero-3-phosphocholine
POPS	1-palmitoyl-2-oleoyl-*sn*-glycero-3-phosphoserine
PRR	proline-rich region
PTMs	post-translational modifications
RT	room temperature
SEC	size exclusion chromatography
SM	sphingomyelin
smFRET	single-molecule Förster resonance energy transfer
SUVs	small unilamellar vesicles
TIRF	total internal reflection fluorescence
β-factor	fraction of donor fluorescence in the acceptor channel
η_x	detection efficiency
I_x	fluorescence intensities
ϕ_x	quantum yield
τ_D	diffusion time
γ	corrector for the difference in the donor and acceptor detection efficiency
s-factor	confocal volume

1 Introduction

1.1 General overview of Huntington's disease

Huntington's disease (HD) is a severe autosomal dominant progressive neurodegenerative disease [1]. HD is caused by a pathological expansion of the CAG trinucleotide repeat, and consequently it belongs to the group of polyglutamine (polyQ) diseases [1]. In this particular case, the CAG repeat expansions occur in the exon 1 of the *HTT* gene (*IT15* gene) located on the short arm of chromosome 4 (4p16.3) [2]. This disorder is rare, inherited and without available cure [1], [3], with an estimated worldwide-prevalence of 5.5-15 in 100,000 persons [3], [4].

In healthy individuals, the CAG trinucleotide expansion contains less than 35 CAG repeats. In the range of 36 to 39 CAG repeats, the onset of HD only happens at a late stage in life and an individual may not even develop any symptoms during the course of its life [5]. Individuals with a CAG repeat length of 40 or greater develop HD (assuming a normal life span) [5]. The CAG repeat length is strongly correlated with the severity and the disease onset. With very large CAG expansions (more than 60), the onset could occur below the age of 20. This is known as juvenile HD and accounts for about 7% of HD cases [6].

The first known description of HD was only given in 1841 by the American physician Dr. Charles Oscar Waters. Dr. Waters wrote a letter describing a syndrome likely to be HD, where he noticed the combination of both motor and cognitive decline, and also its hereditary nature [7]. HD was described in further detail in 1872 by Dr. George Huntington, when he published a report in *The Medical and Surgical Reporter* titled "On Chorea" [8]. In this report, Dr. Huntington described the hereditary nature, the early death, the start in adult life, the progression of the incapacity, the link between chorea and dementia, the inappropriate and uninhibited behavior, the recurrent suicides and the absence of treatment [7]. Remarkably, almost a century later, in 1955, the Venezuelan physician Dr. Americo Negrette published a book describing communities in the Venezuelan village of San Luis with high prevalence of HD (700 per 100,000 persons). This discovery led to a strong interest in HD and the formation of The Venezuela Huntington's Disease Project, establishing a network of social support and the subsequent discovery of the linkage of HD to the *HTT* gene in chromosome 4 [7].

Like other neurodegenerative diseases, HD displays some of the typical symptoms, which evolve and progress over time. In an early stage of the disorder, some manifestations include changes in personality and cognition, in which mood swings, irritability and depression can occur. Afterwards, the symptoms progress to the appearance of chorea, which is a movement disorder, causing abnormal, involuntary and non-repetitive movements [9]. Chorea is characterized by irregular contractions that appear to flow from one muscle to the next, and is caused by an overactivity of dopamine in the areas of the brain that are responsible for movement [9]. Overtime, the symptoms become more severe and voluntary activity becomes increasingly difficult. Outbursts of aggressive behaviors and social disinhibition are also frequent in later stages of the disease.

1.1.1 Huntington's disease diagnosis and symptoms

The diagnosis of HD is based on the individual's family history or on the genetic tests for the detection of the CAG repeat expansion in the *HTT* gene [5], [10]. Tests for the onset of motor disturbance could also be performed using a calculated score defined by the Unified HD Rating Scale. This scale

includes motor, cognitive, behavioral, emotional, and functional components, in which all are considered with a subscale of diagnostic confidence. This score ranges from 0 (no motor abnormalities suggestive of HD) to 4 (≥99% to be due to HD), with a score of 4 to be a manifestation of HD [10].

Most symptoms of HD become noticeable between the ages of 30 and 50 years, but they can begin earlier in juvenile HD [11]. In about half of the HD cases, the psychiatric symptoms appear first. Their progression is often divided into three stages: early, middle, and late stages. In the first, there are subtle personality changes, problems in cognition, irritability, and mood swings, all of which can be overlooked at first glance. The motor symptoms usually evolve in the middle stage, but the onset, progression and extent of the cognitive and behavioral symptoms vary significantly between individuals [11]. During the middle stage, it appears involuntary and inability to control speed and force of movements, chorea (jerky, random movements), equilibrium problems, slow reaction time, weight loss, speech difficulties and stubbornness [5]. All these symptoms are progressive and worsen over time, eventually leading to a complete dependency of the HD patient to constant care in the later stage. During this stage, there is rigidity in the body, severe chorea, significant weight loss, inability to walk, speak and difficulties in swallowing [5]. In juvenile HD, the symptoms usually progress at a faster rate with a greater cognitive decline, but chorea is usually not exhibited [12].

In addition, as the cognitive abilities are continuously degrading, this usually leads to dementia. This is mainly due to the effect of the mutant huntingtin (mHTT) in the neural cells, causing problems in memory, thinking and neural functions in general [1]. Overall, HD has a significant impact on patients and families, imposing significant physical, emotional, and financial burdens. People with HD often need extensive support for daily activities and may end up having to move to permanent healthcare facilities. Since HD has a genetic basis, it poses moral questions for affected individuals and their relatives: genetic testing can detect the presence of the disease, triggering concerns about matters like reproductive decisions and insurance bias.

1.2 The huntingtin protein

Huntingtin (HTT) is found in many of the body's tissues but it is mainly expressed in the brain cortex (the cerebellar cortex, the neocortex, the hippocampal formation, and the striatum), more specifically in the cytoplasm of neurons [13], [14]. The HTT protein is coded by the *HTT* gene, and its precise function is currently unknown. However, recent studies support the idea that the HTT protein can function as a molecular "hub", meaning that the protein binds to different proteins into complexes or it promotes their dissociation, providing a vital control of distinct cellular processes [1]. Specifically, HTT is mainly associated with cellular membranes, contributing to the dynamics of the vesicular transport, synaptic transmission and regulation of autophagy and embryogenesis [1], [15]. Moreover, HTT likely plays a critical role in the development and formation of the central nervous system (CNS) by inhibiting apoptosis. In mice, the depletion of HTT results in embryonic lethality, and a 50% reduction in its expression levels leads to abnormal brain development [16], [17]. Further studies suggest that HTT's anti-apoptotic function seems to be linked to its ability to sequester pro-apoptotic proteins and/or inhibit specific caspases [18], [19].

HTT is a soluble, mostly cytoplasmic, and a large multidomain protein with a molecular weight of 350 kDa (more than 3000 amino acids) [11]. The Nt17 domain is located in the N-terminal region of the HTT protein. This domain is composed of 17 amino acids (mostly conserved between vertebrates) and forms an amphipathic α-helix upon interaction with lipid membranes [15], [20]. It functions as a cytoplasmic retention signal and is subject to several post-translational modifications (PTMs) [21]. Following this domain, the polyglutamine (polyQ) stretch contains the sequence of the CAG trinucleotide repetitions, whose length in mHTT is highly related to the severity and the HD onset. The proline-rich region (PRR) follows the polyQ domain. The PRR is only present in mammals, which suggests that is very recent in terms of evolution of the HTT protein [22]. Even though this domain seems to be important for mediating protein-protein interactions (since it is critical for interactions with proteins that contain tryptophan or SH3 domains [23]), it is highly variable between individuals and its deletion had no severe effect on mouses [15], [24]. In the C-terminal location of HTT, a nuclear export signal has also been identified [21].

In the mutant form, mHTT is thought to be toxic due to a gain-of-function mutation, which confers to it an enhanced probability of the protein to aggregate. mHTT is more prone to cleavage and to aberrant splicing, that create shorter fragments that can aggregate and form inclusion bodies in the cytoplasm, interfering with the normal cellular function. In brains, N-terminal fragments of mHTT has been found post-mortem, suggesting that this region is a key step in the development of HD [18], [25], [26].

Until recently, few structural data were available for the full-length HTT. In a recent study, Qiang Guo *et al*. [27] obtained the HTT17Q (with a polyQ extension of 17 glutamines) structure in complex with the HTT-associated protein 40 (HAP40) protein with an overall resolution of 4 Å by cryo-electron microscopy (Cryo-EM). HAP40 was used to stabilize the HTT structure, and tightly binds to HTT in a cleft formed by two larger domains rich in HEAT repeats [27], [28]. The HTT protein used to determine the structure in the previous article was co-expressed in B1.21 human cells (B1.21-HAP40TS) with the HAP40 protein. Remarkably, this work revealed that HTT protein has three major domains: the N- and C-terminal domains containing multiple HEAT repeats – huntingtin, elongation factor 3, protein phosphatase 2A and lipid kinase TOR (N-HEAT and C-HEAT, respectively); and a small bridge domain linking both N-and C-HEAT. However, in this work, some segments of HTT were still left unresolved, including the N-terminal that contains the Huntingtin exon 1 (Httex1). It appears that the disordered regions are mostly accessible to protease action and to PTMs that might modulate protein-protein interactions [27].

HEAT repeats are protein tandem repeats forming a structural motif composed of two α-helixes. They are usually involved in intracellular transport and regulation, but their function can be highly variable. The HEAT repeat domains may function as scaffold for numerous protein complexes, mediating inter- and intra-molecular interactions [15].

The N-HEAT (residues 91-1,684) contains 21 HEAT repeats in a typical α-solenoid structure, adopting a one-and-a-half-turn right-handed superhelix [27]. The highly toxic Httex1 fragment is located in this domain. The C-HEAT (residues 2,092-3,098) includes 12 HEAT repeats arranged in an elliptical ring. Besides the flexible linkage of the bridge connecting both the N-HEAT and the C-HEAT domains, there is a weak loop interactions between these two domains which might explain the highly dynamic

structure of HTT in the absence of a binding partner (such as HAP40) [27]. Figure 1.1 shows the Cryo-EM structure of the HTT-HAP40 complex.

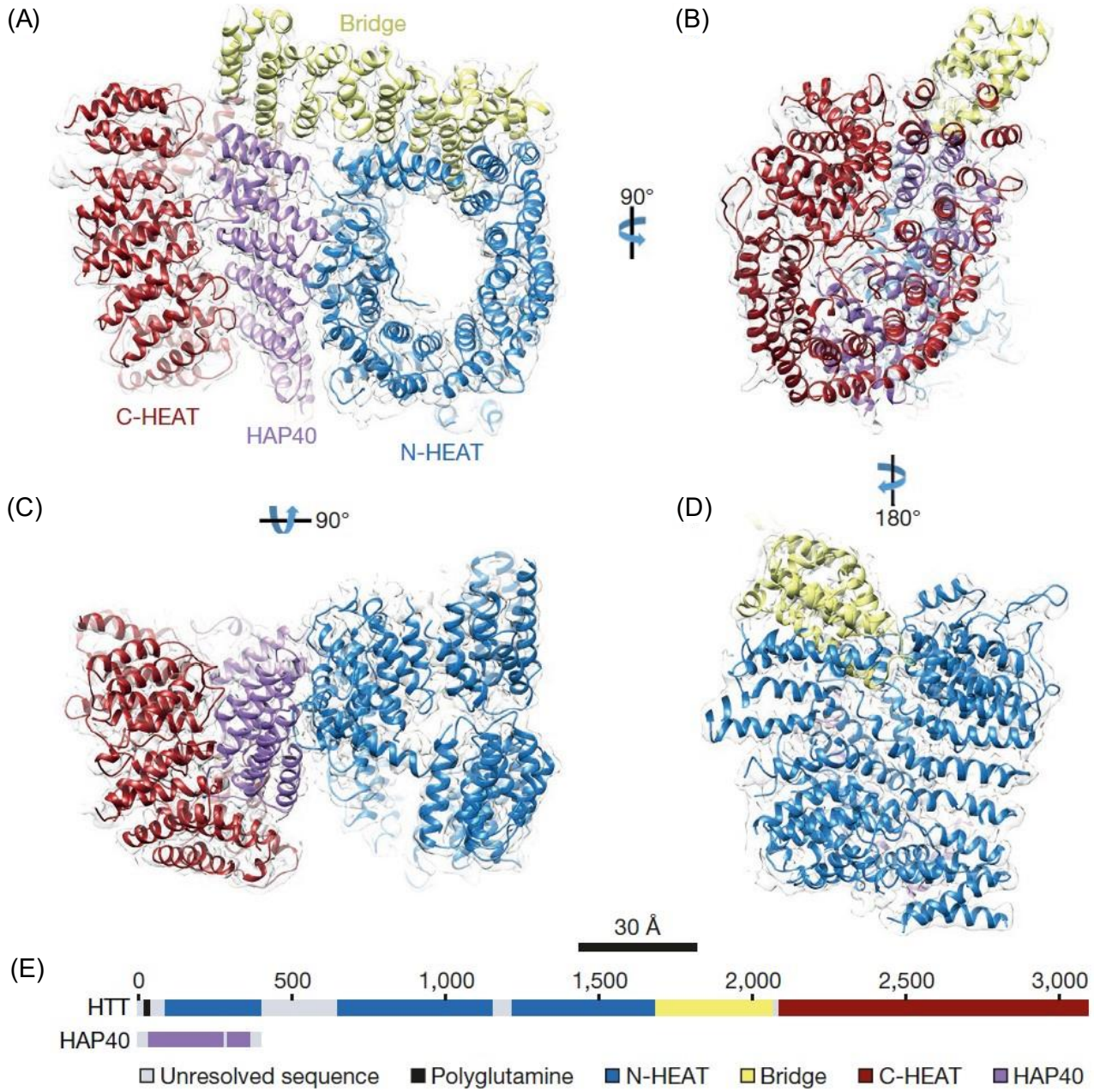

Figure 1.1 – The CryoEM structure of the HTT–HAP40 complex. (A-D) Different views of the HTT–HAP40 complex. The density map filtered to local resolution is illustrated as a translucent surface. The ribbon representation is color-coded by domain: HTT N-HEAT domain-blue; HTT bridge domain-yellow; HTT C-HEAT-maroon; and finally, HAP40-purple. (e) Representation of the domain organization of both HTT and HAP40 proteins forming the complex. Reproduced from [27].

1.2.1 HTT interaction with other proteins

HTT shows some sequence homology with other proteins and is expressed ubiquitously in all tissues, but with high levels in the central nervous system. HTT is located in the nuclei, cell bodies, dendrites and nerve terminals [23]. In addition, HTT interacts with distinct proteins that control vesicle

trafficking and cytoskeletal anchoring, clathrin-mediated endocytosis, neuronal transport, postsynaptic signaling, anti-apoptosis stress and neuronal gene transcription regulation [23], [29].

The 14-3-3 proteins are a family of highly conserved regulatory molecules that are expressed in eukaryotic cells and control the actions of other proteins participating in the cell cycle regulation, transcriptional control, signal transduction, intracellular trafficking, ion-channel regulation, and apoptosis [30]. Their role is not exactly understood but they seem to modulate the subcellular localization of proteins and function as adaptor molecules, accelerating interactions between kinases, receptors, enzymes and cytoskeletal proteins. These proteins are highly expressed in brain cells, and the expression changes depending on their isoforms, cell types and the region in which they were expressed [30]. In the study of Omi *et al*. [30], it was revealed that the aggregate formation of the Httex1 that contains an expansion of polyQ was dependent on the correct expression of 14-3-3zeta, since the suppression (by a small interfering ribonucleic acid (siRNA)) of the expression of these proteins completely abolished the formation of mHTT large inclusion bodies [30]. Figure 1.2 shows HTT domains and sequence comparison for different species, in addition of examples of HTT interactions with other partners.

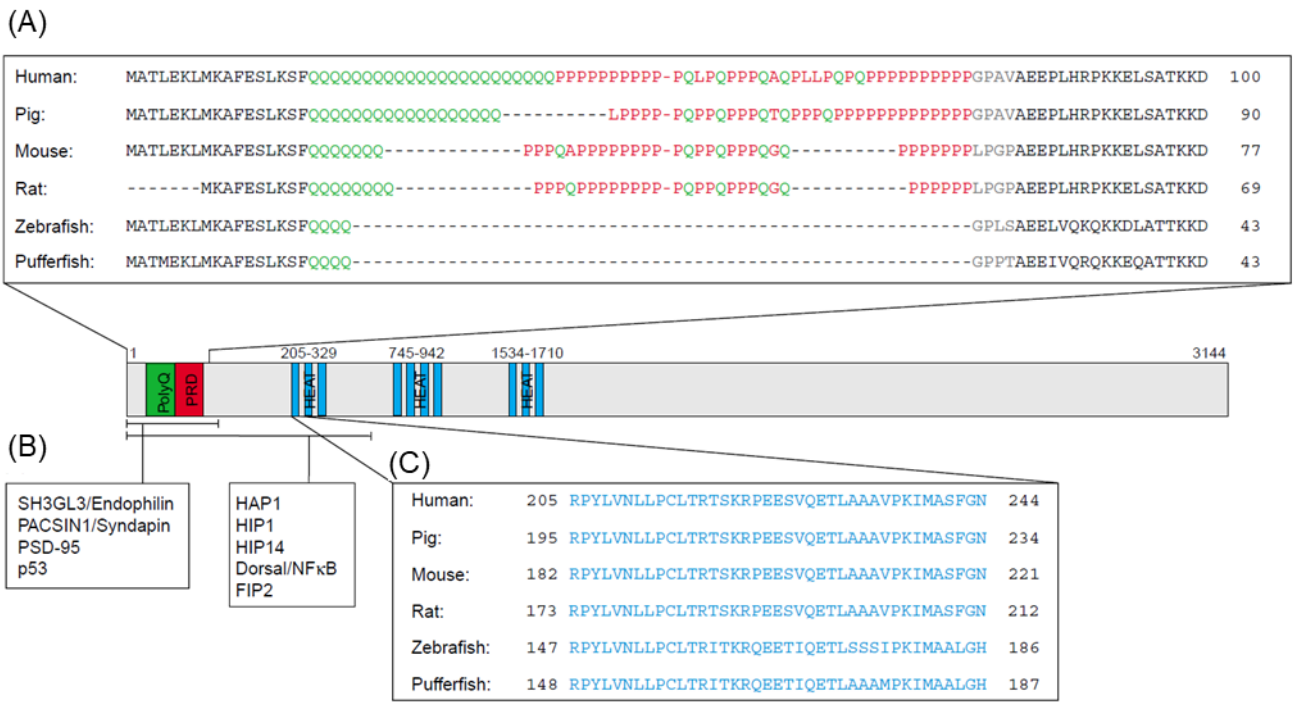

Figure 1.2 – HTT domains and sequence comparison across different species. (A) HTT contains a glutamine/proline-rich region at the N terminus and (C) ten HEAT repeats clustered in three domains in the N-terminal half of the protein. (B) Examples for HTT interaction partners identified for the glutamine/proline-rich region at the N terminus and the first cluster of HEAT repeats are listed. Amino-acid-sequence comparison of HTT between different species (human 454415, pig 4126796, mouse 1708161, rat 1708162, zebrafish 2981138 and pufferfish 804981) shows that (A) the glutamine/proline-rich region at the N terminus is only partially conserved, whereas (B) the HEAT repeats are highly conserved. Reproduced from [23].

1.3 Httex1

The first exon of the HTT is usually called by Httex1. Httex1 is the most studied part of the HTT protein. This fragment is usually generated either by an aberrant splicing event in which the mRNA transcript originated from *HTT* gene is involved, or by the proteolysis of the full-length HTT. Figure 1.3 contains a schematic illustration of the expression of *HTT* and the formation of Httex1.

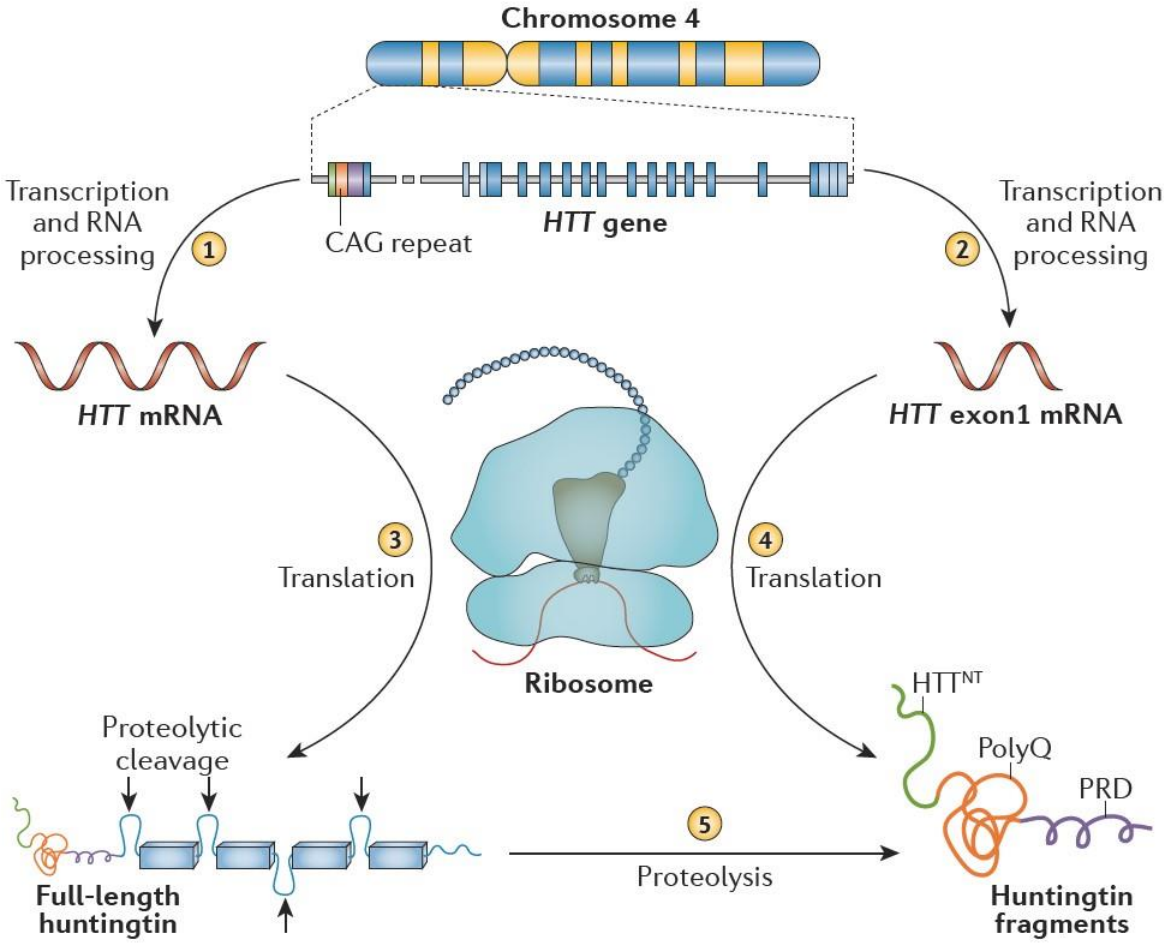

Figure 1.3 – HTT expression and origin of Httex1. (1) The *HTT* gene is expressed normally and a full-length *HTT* mRNA is generated and (3) it is translated into a full-length HTT protein. (2) An aberrant splicing event generates a mRNA that encodes for just the Httex1, (4) which is then translated to a HTT fragment, Httex1. (5) The full-length HTT can suffer proteolytic cleavage in specific sequences (indicated by arrows) originating HTT fragments, including Httex1. Reproduced from [31].

Httex1 comprises three major domains: the N-terminal 17 amino acid domain (Nt17 segment), the polyQ tract, and finally the C-terminal PRR. All of these domains are highly disordered in solution and are able to modulate the misfolding, oligomerization and fibrillation of both Httex1 and the full-length protein [27].

The Nt17 domain (Figure 1.4) undergoes several PTMs, such as phosphorylation (3, 13 and 16 residues), acetylation and ubiquitination in HD brains [32]. Moreover, the α-helical content seems to increase with the polyQ extension, that afterwards can form β-sheet-rich fibrils by self-assembly of

different Httex1 monomers [33]. Some studies also suggest that Nt17 domain plays a critical role in HTT aggregation and interactions with binding partners, subcellular location and toxicity [32], [34]. Figure 1.4 shows a schematic of the HTT and the Httex1.

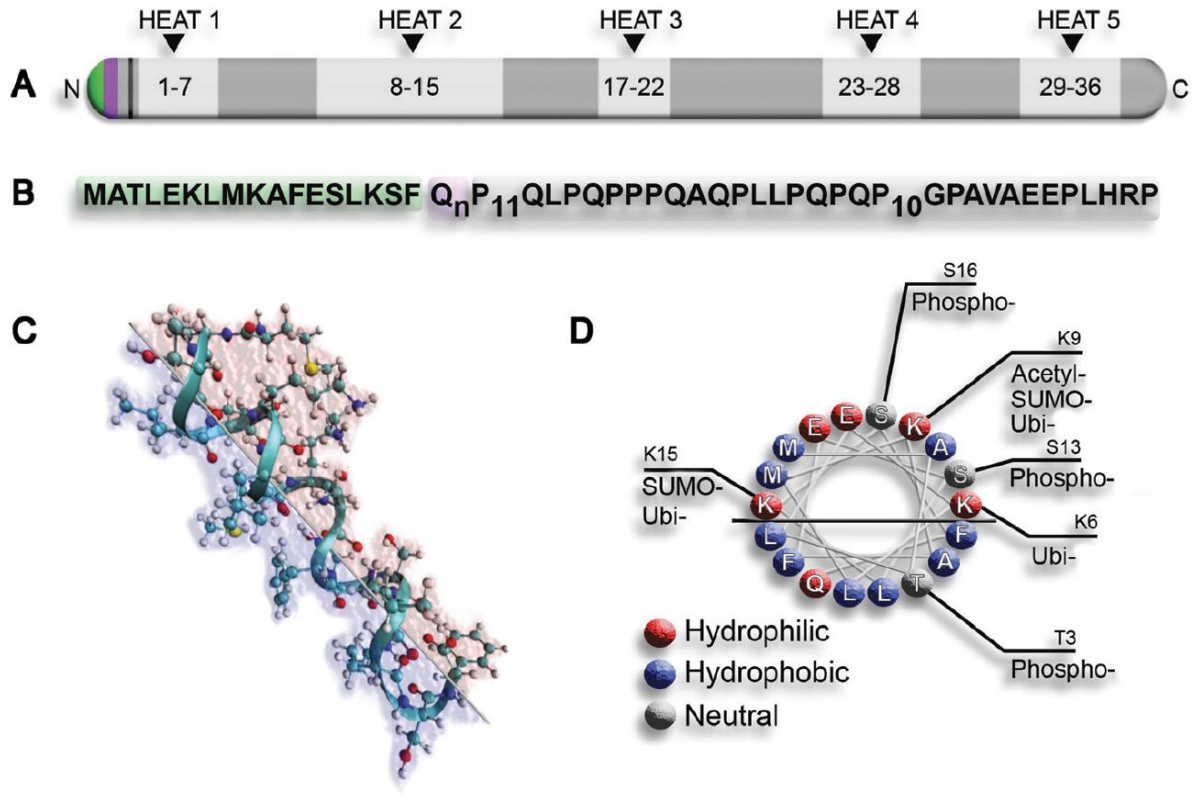

Figure 1.4 – Schematic representation of the HTT protein, Httex1 and the Nt17 domain. (A) The full-length HTT protein with the HEAT repeat sites. (B) The amino acid sequence of the Httex1, showing the Nt17 domain (green), the polyQ domain (purple) and the PRR (grey). (C) A theoretical 3D structure of the Nt17 segment, showing the hydrophilic (red) and hydrophobic (blue) faces of the amphipathic α-helix. (D) View from down the barrel of the α-helix, with the hydrophobicity of each residue highlighted, and the site of reported PTMs. Reproduced from [20].

Previous studies found that the overexpression of N-terminal fragments of HTT, is enough to induce many of HD features in mice [24], suggesting that these fragments are critical to the development of the disease and its pathogenicity. The Nt17 domain also includes a functional nuclear export signal (NES) that may regulate the cellular localization and trafficking of HTT. Abnormal expansion of the polyQ or specific mutations within the Nt17 domain results in HTT accumulation within the nucleus and is a source of cytotoxicity. Although the polyQ-flanking regions are highly conserved throughout mammalian evolution, they do not appear to be necessary for the normal function of HTT. Rather, the flanking regions may have co-evolved with polyQ stretches to modulate their pathogenicity, as indicated by their significant involvement in the aggregation toxicity of mutant HTT [18]. The PRR domain contains a polyproline II (PPII) helix which is a relatively rigid structure that may be important in stabilizing the structure of the polyQ domain [15], [35].

The expanded polyQ domain is responsible for the formation and the deposition of intranuclear and cytoplasmic inclusion bodies formed by fibrillar HTT aggregates. After the discovery of this

phenotype and disease features, it was hypothesized that the formation of the inclusion bodies was the main cause observed in the HD pathology [36]. However, recent studies have challenged this hypothesis, demonstrating that the inclusion bodies might be either a protective, while the smaller and more diffuse aggregates may represent the toxic entities [15], [37]–[39]. Figure 1.5 displays a summarized schematic of the aggregate's formation process.

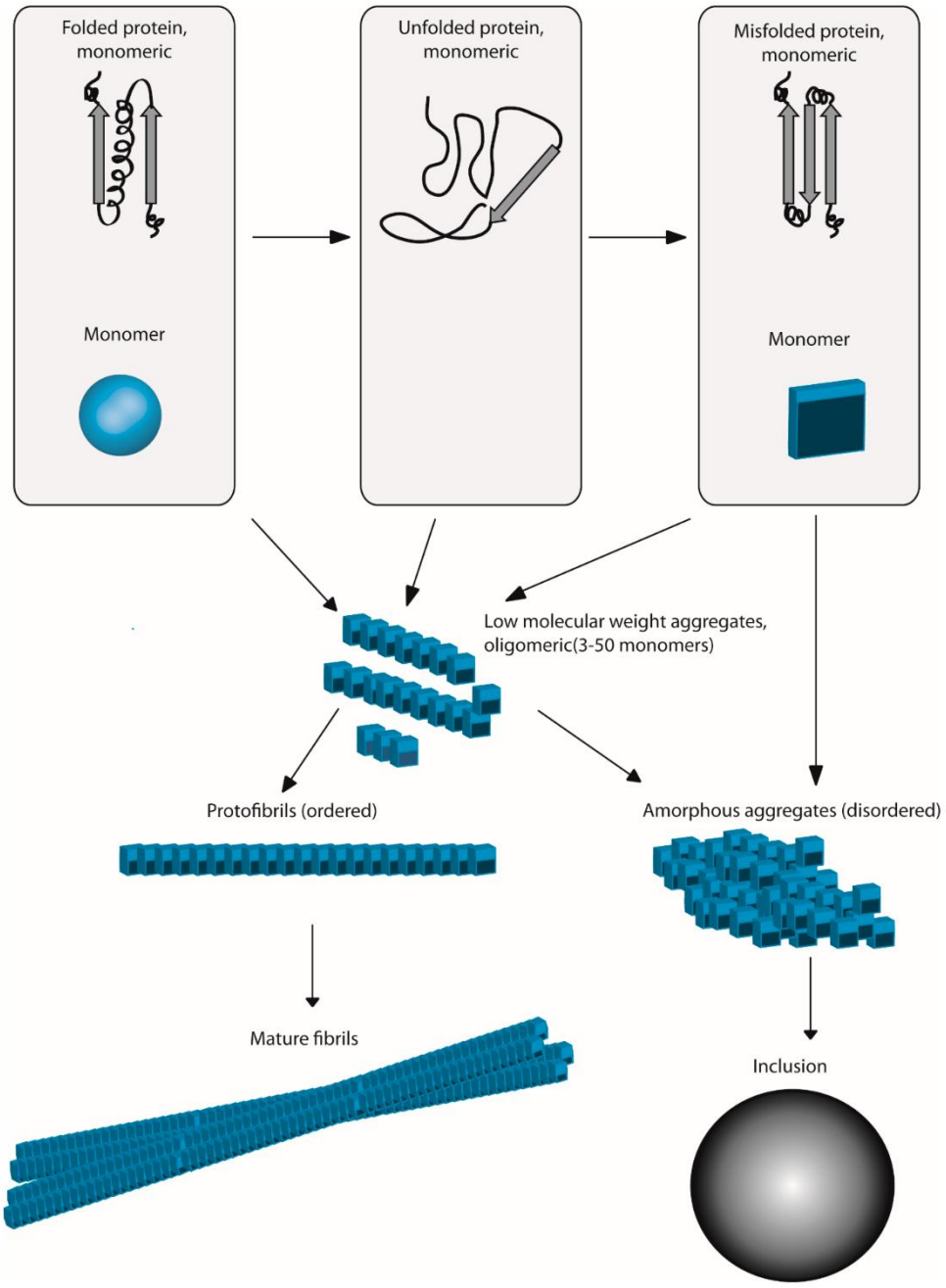

Figure 1.5 – General overview of the protein aggregation progress. Folded monomers can aggregate by its unfolded or misfolded monomer structure. Folded monomers can also aggregate from native-like conformations, skipping the unfolded step. The association between several monomers leads to the formation of oligomeric species with low molecular weight. The continuous addition of oligomers can happen in a structured manner, leading to the formation of protofibrils and mature fibrils. The precipitation of monomers or oligomers leads to the formation of amorphous aggregates, resulting in protein inclusion bodies. Reproduced from [40].

1.4 Httex1 interaction with lipids

HTT is involved in orienting miotic spindles during cell division [41], transporting vesicles along the microtubules [42], and association with lipid membranes from the endoplasmic reticulum (ER) [43], [44] and nucleus [45]. The first domain of the Httex1 (the Nt17 domain) has been shown to adopt a highly conserved amphipathic α-helix upon membrane binding, showing its role in Httex1-lipid interaction [43]. In fact, the interaction and insertion of the HTT with membranes has been demonstrated to be polyQ dependent, supporting the hypothesis that the availability of the Nt17 domain may be essential for the modulation of Httex1-lipid interaction [37].

PTMs of HTT have been shown to modify its function and interaction with cellular membranes. In fact, the PTMs that appears to make a bigger difference in the HTT-lipid interaction, seems to be located in the Nt17 domain. One study showed that phosphomimetic mutations at serine 13 and serine 16 reduced the fibril formation kinetics, but there was an accumulation of alternative aggregates [37], [46]. In this study, the intraventricular infusion of ganglioside GM1 induced the phosphorylation of the serine 13 and 16 at the Nt17 domain, attenuating the mHTT toxicity and restoring most of the motor function [46]. As another structural study has indicated, it appears that phosphorylation of the serines 13 and 16 brings a change in the amphipathic α-helix, inhibiting it and as a consequence it alters the location of HTT in the cells [47], [48]. Figure 1.4 shows the sites in which PTMs have been reported to occur.

Sumoylation modifications within Nt17 domain have been shown to alter the HTT location and the trafficking HTT to the nucleus. In addition, this PTM in the mHTT has also demonstrated increased the amount of the soluble diffuse aggregates and inclusion bodies, responsible for the greater toxicity in neural cells of HD *Drosphila* models [49], [50]. Another study showed that more specifically, when Rhes, a protein selectively localized in the striatum that increases sumoylation in transgenic mice, is overexpressed in mHTT knock-in striatal cell, the cell survival rate was reduced by 60% when compared to the effect with wild-type HTT, which suffered no effect [50], [51].

In a study by Kathleen A. Burke *et al*. [34], the authors demonstrated that the flanking sequences directly adjacent to the polyQ domain, such as the Nt17 domain and PRR, heavily influence the HTT aggregation. They employed atomic force microscopy (AFM), Langmuir trough techniques and vesicle permeability assays to directly monitor the membrane interaction of several synthetic polyQ peptides with different combinations of flanking regions (some with and/or without the Nt17 and the PRR). One of the main observations was that the polyQ peptides that lacked the Nt17 domain did not insert into lipid membranes and neither appreciably aggregate [34]. As noted by the authors, this is a great indicator that the polyQ domain alone is not enough to induce aggregation states and inclusion bodies. In this same study, they demonstrated that lipid membranes can stabilize specific aggregate structures of polyQ peptides that just contain the Nt17 domain [34]. This domain also seems to impact on the first glutamines of the polyQ domain to adopt an α-helix conformation, just like this conformation has been observed for the Nt17 domain. In addition, an increase in the α-helix content with longer polyQ domain-lengths was detected by circular dichroism [33], [34]. The importance of the amphipathic α-helix domain has been shown to be a facilitator of the mechanisms of interaction between amyloid-forming proteins

and lipid membranes. Nevertheless, further clarification of the impact of polyQ expansion on the structure and stability of the Nt17 domain is still required [34].

The aggregation rate of the polyQ peptides studied in the previous study seems to be dependent on the flanking sequences. Additional support for the importance of the PRR region on the HTT aggregation was also observed here, as different aggregation morphologies were shown between peptides with and without the PRR sequence, on the lipid bilayer. In addition, the PRR domain seems to have caused larger and amorphous aggregates to form on membranes when the Nt17 domain was present, which is an indicator that the PRR domain enhances the interaction between Httex1 and lipid membranes. This is further confirmed by the appearance that the presence of the PRR domain softens the bilayer surface locally, probably due to the influence that the PRR sequence has on the conformation of the polyQ domain. This also explains the difference in the rates of fibril aggregation when it is or is not present, being slower when the PRR domain is present [52]. The presence of the PRR also seems to facilitate the ability of the Nt17 domain to associate specifically with the ER and the Golgi apparatus [34], [53]. In Figure 1.6 the impact of the flanking regions on the kinetics of mHTT aggregates is represented.

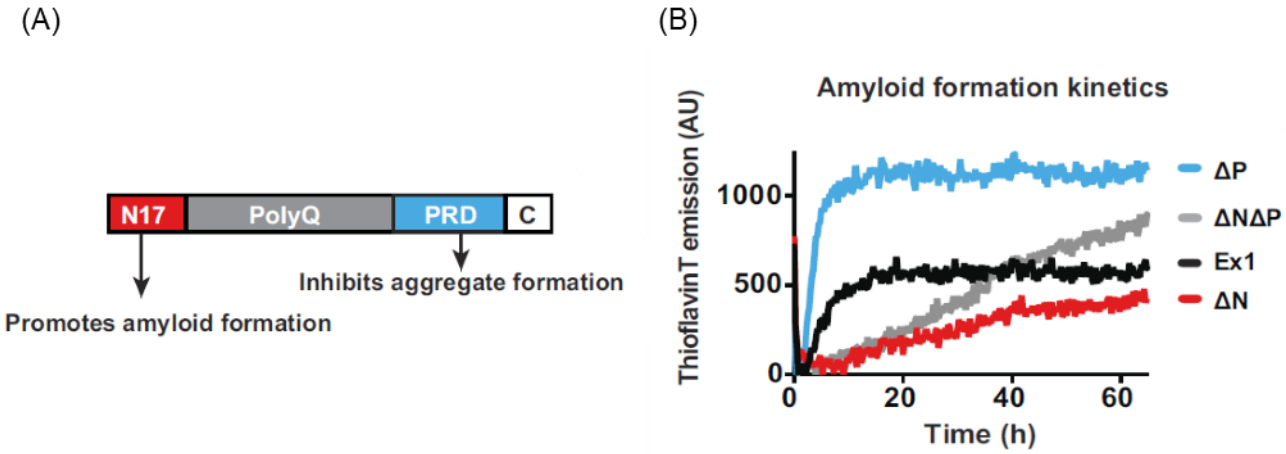

Figure 1.6 – Flanking regions impact pathogenic mHTT aggregation propensity. (A) Summary model of how the Nt17 domain and PRR contribute to mHTT aggregation propensity. (B) The rate of accumulation of amyloid aggregates for mHTT variants. Aggregates without the Nt17 domain (ΔN and ΔNΔP) aggregate much slowly than the ones with the Nt17 region (Ex1 and ΔP). Reproduced from [54].

The interaction between HTT and lipid membranes might be responsible for the observable aggregate pathogenesis present in HD. This can be because this interaction can stabilize and promote the formation of specific aggregate toxic species since anchoring to membranes may lead to high local concentration of peptides that facilitate such aggregation [34]. In that case, PTMs on the Nt17 domains that reduce the affinity of it to the lipid membranes, might alleviate the toxicity observed and be responsible by the apparent diminutive pathogenesis [34], [47]. The flanking domains (PRR and Nt17) which are directly adjacent of the polyQ domain are then a potential target for therapeutical strategies which might help neutralize the toxicity of mHTT aggregates. However, more research is needed in order to reach that objective, including research in how the existence of different conformers mediate the

pathogenesis in HD and what is the role of different environmental factors on how they affect those conformers. Membrane elasticity directly influences membrane stability and an alteration to this property might lead to dysfunction of the cell and the consequent disease [34], [55], [56].

In the study by M. Tao, *et al.* [57] the authors hypothesized that, since the Nt17 domain is positive-charged due to the existence of three lysine residues and two glutamic acid residues, this positive net-charge would promote binding with negatively-charged membranes. The researchers tested this theory by using small unilamellar vesicles (SUVs) containing 1-palmitoyl-2-oleoyl-*sn*-glycero-3-phosphoserine (POPS) and 1-palmitoyl-2-oleoyl-*sn*-glycero-3-phosphocholine (POPC) in a molar proportion of 25:75. Their results indicated that electrostatic interactions did indeed modulate the binding events of Httex1 with lipid membranes since increasing amounts of the negatively-charged lipid POPS would strongly enhance membrane binding, but they also make a note that binding still occurred at lower extents with vesicles containing only the neutral-charged lipid POPC.

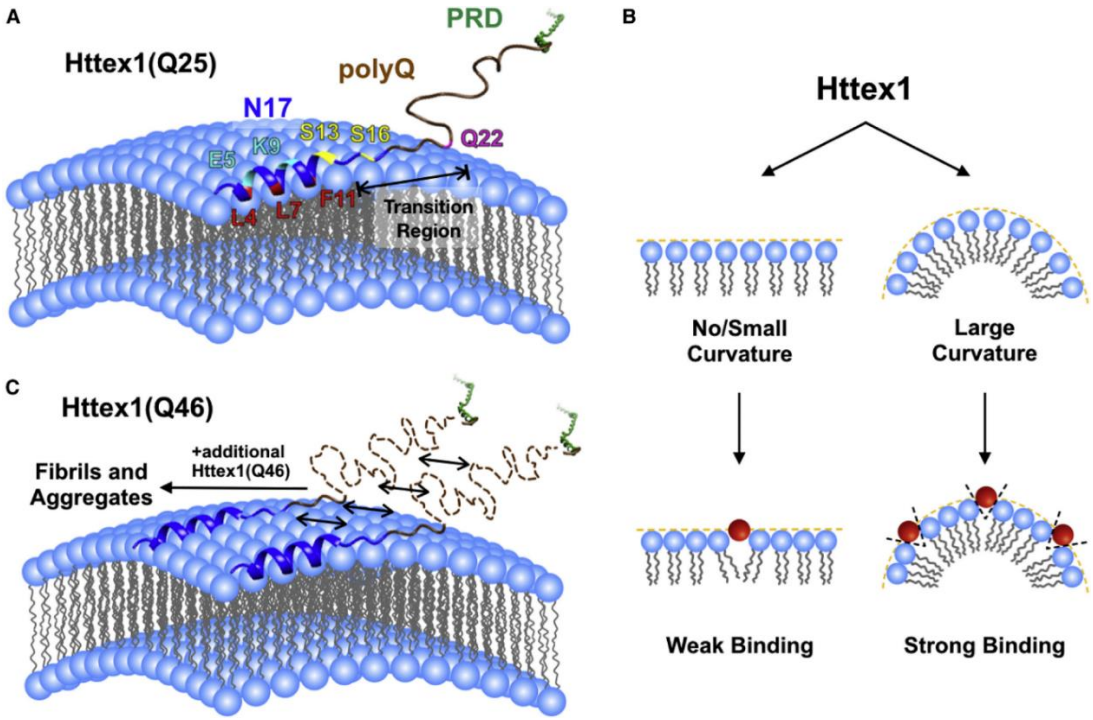

Figure 1.7 – Schematic illustration of the interaction between Httex1 and lipid membranes. (A) The image depicts the interaction between Httex1-25Q and curved membranes. Different domains of the protein are color-coded: the PolyQ and PRD domains are brown and green, respectively. The Nt17 domain is blue with highlighted residues: cyan highlights indicate selected solvent-exposed residues (E5 and K9), red highlights represent selected membrane-exposed residues (L4, L7, and L11), yellow highlights denote phosphorylation residues (S13 and S16), and magenta represents Q22. The ribbon representation shows the α-helical structure of residues 3-13. The transition region (14-22) is formed by the C-terminus of Nt17 and the N-terminus of the polyQ domain, while the remaining part of the protein (residues 23 onwards) is completely exposed to the solvent. (B) The diagram illustrates the preferential interaction of the N-terminal Httex1 helix (represented by a red circle) with curved membranes. Vesicles with positive membrane curvature exhibit greater defects in lipid packing in the head-group region, creating a more favorable environment for the helix to bind to the membranes. (C) The image demonstrates the membrane-mediated aggregation of Httex1 with an extended polyQ region, represented by Httex1-46Q. Monomeric Httex1-46Q molecules collide with each other on the membrane, and the polyQ regions from different molecules come into contact, initiating the formation of intermolecular β-sheet structures. This process ultimately leads to the formation of fibrils and aggregates. The color code for the protein domains is the same as in (A). Reproduced from [57].

Despite HTT having a prominent membrane location, there is still not much knowledge about the relationship of HTT with lipids and their role in HD. Some studies have shown a reduced cholesterol levels in numerous HD models, caused by a transcriptional deregulation of the cholesterol pathway [58]. Changes in the ganglioside GM1, which is found in membrane rafts and affects signaling pathways, have also been found and determined to alter the transcription of metabolic enzymes.

1.5 Goals and experimental strategy

The pathophysiological mechanism of HD remains unknown, but accumulated evidence supports that Httex1 binds to lipid membranes and aggregates at its surface, contributing for Httex1 cytotoxicity. However, the effects of the membrane physical properties in this interaction remain poorly under-stood.

The specific aims of this project were:

(i) to quantify the binding of Httex1-23Q to lipid vesicles with distinct compositions.

(ii) to characterize the role of each flanking polyQ region – N-terminal Nt17 and C-terminal PRR – in the Httex1-lipid interaction.

Tag-free Httex1-23Q was produced using a SUMO-fusion strategy. Several constructs were created: (i) Httex1-23Q-A2C or -A82C (probing Nt17 and PRR, respectively) labeled with Acrylodan or Atto 488 maleimide, and (ii) a double-labeled Httex1-23Q-A2C/A82C with Alexa 488 and 594 maleimide for smFRET.

The thesis was organized in three major work plans:

- Evaluate the Httex1-lipid interaction and the role of each flanking polyQ region by Acrylodan fluorescence (reports on local polarity). Steady-state and time-resolved fluorescence measurements of Httex1-23Q-A2C-Acrylodan in solution and upon increasing lipid concentrations (LUVs composed of pure POPC and 1:1:1 SM:Chol:POPC) were performed. The same strategy was also applied for Httex1-23Q-A82C-Acrylodan (also using LUVs composed of 25:75 POPC:POPS).
- Characterize the conformational dynamics of PRR and Nt17 in the Httex1 membrane-bound state. Fluorescence anisotropy decays of both Httex1-23Q-A2C and -A82C labeled with Atto 488 in buffer and in the presence of 1mM LUVs were carried out.
- Calibration of the smFRET step (10-mer dsDNA and Z-position of optical fibers). First measurements of double-labeled Httex1-23Q-A2C/A82C were performed.

2 Materials and methods

2.1 Plasmid, materials, and reagents

The pET-SUMO-Httex1-23Q plasmid was previously cloned in the host lab. Briefly, the Httex1-23Q cDNA was obtained from the pTWIN1-His_6-Ssp-Httex1-23Q plasmid (a gift from Hilal Lashuel – Addgene plasmid # 84349 [59]) and then inserted into a pET SUMO vector (Invitrogen). BL21(DE3) One Shot® chemically competent *E. coli* was obtained from Thermo Fisher.

Luria Broth (Miller's LB Broth), isopropyl ß-D-1-thiogalactopyranoside (IPTG), dithiothreitol (DTT), kanamycin (Km), BlueSafe and NZYColour Protein Marker II were purchased from NZYTech. The cOmplete Mini EDTA-free Protease Inhibitor Cocktail Tablets are from Roche. Phenylmethylsulphonyl fluoride (PMSF) was obtained from PanReac AppliChem. Amicon® Ultra-15 Centrifugal Filters with 3 and 10 kDa cutoff were purchased from Millipore. 0.44 µm syringe filters (low protein binding) are obtained from Labbox. The Modified Lowry Protein Assay Kit, Pierce™ BCA Protein Assay Kit is from Thermo Fisher. The 5-mL HisTrap FF, 5 mL-HiTrap desalting, and Superdex 75 10/300 GL columns were obtained from GE Life Sciences.

The 1-palmitoyl-2-oleoyl-*sn*-glycero-3-phosphocholine (POPC), 1-palmitoyl-2-oleoyl-*sn*-glycero-3-phosphoserine (POPS) and sphingomyelin (SM) are from Avanti Polar Lipids, while cholesterol (Chol) is from Sigma (Figure 2.1). The lipid stock solutions were prepared in chloroform spectronorm (VWR) and their concentrations (except for cholesterol) were determined by the phosphate analysis method adapted from McClare [60]. The lipid stocks were stored at -20ºC until further use.

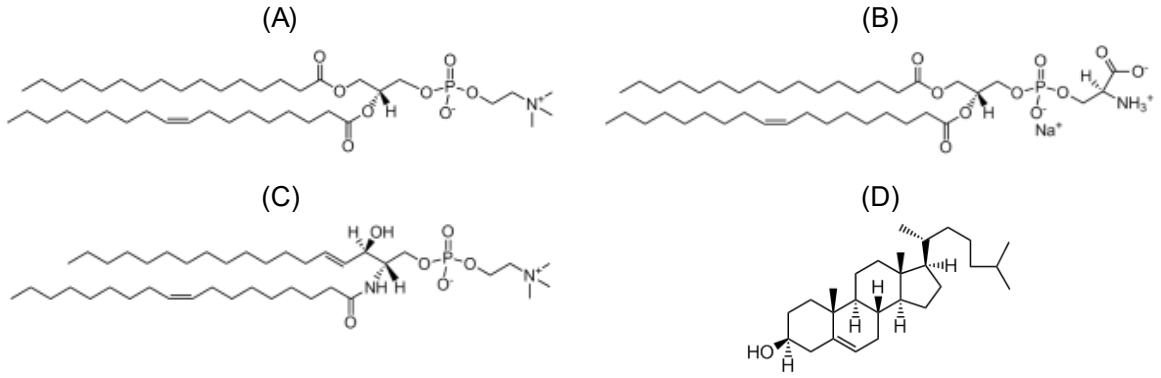

Figure 2.1 – Chemical structures of the lipids and sterol used in this work. (A) 1-palmitoyl-2-oleoyl-*sn*-glycero-3-phosphocholine (POPC), (B) 1-palmitoyl-2-oleoyl-*sn*-glycero-3-phosphoserine (POPS), (C) 18:1 sphingomyelin (SM) and (D) cholesterol (Chol). Adapted from [61].

The fluorescent probes 6-acryloyl-2-dimethylaminonaphthalene (Acrylodan), Alexa Fluor™ 488 C_5 maleimide (Alexa 488) and Alexa Fluor™ 594 C_5 maleimide (Alexa 594) were obtained from Invitrogen and Atto 488 maleimide (Atto 488) is from Sigma. The oligonucleotides labeled with Alexa 488 (A488N – 5'CGGATCTCGG) and Alexa 594 (A594N – 5'CCGAGATCCG) were synthesized by Integrated DNA Technologies.

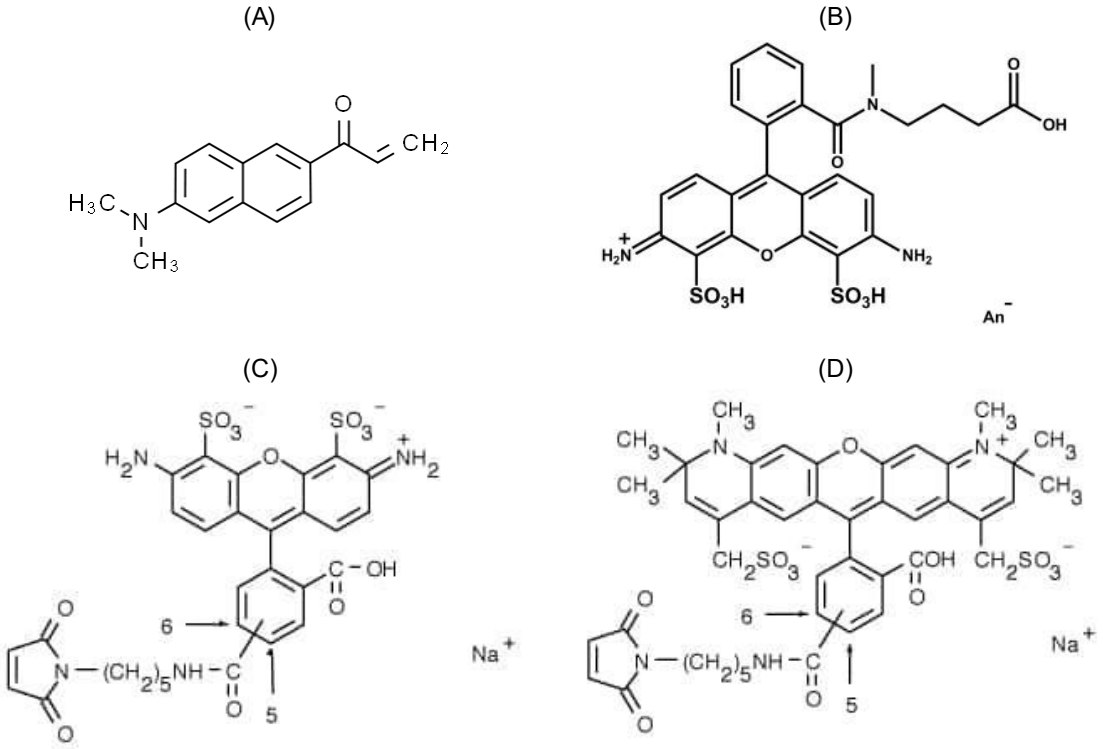

Figure 2.2 – Chemical structures of the fluorescent probes used in this work. (A) Acrylodan, (B) Atto 488, (C) Alexa 488 maleimide and (D) Alexa 594 maleimide. Adapted from [62].

The chemicals used for the preparation of buffers/solutions during the protein expression/purification and the fluorescence measurements were acquired from Sigma or Thermo Fisher. Reagents for SDS-PAGE gels are from NZYTech. Buffers were prepared with Milli-Q water (18.2 MΩ·cm), always filtered with 0.2 µm membrane filters (Sartorius), and final stored at 4 ºC.

2.2 Production of single- or double-labeled Httex1-23Q constructs

In the scope of this thesis, several constructs were created: (i) single-labeled Httex1-23Q constructs at position A2C or A82C with Acrylodan or Atto 488 maleimide, and (ii) a double-labeled Httex1-23Q construct at positions A2C and A82C with Alexa 488 and 594 maleimide. The procedures described below for the recombinant expression and purification of Httex1-23Q were applied to all constructs. Only the labeling was adapted according to previous publications [63]–[65].

2.2.1 Expression of the fusion protein His_6-SUMO-Httex1-23Q

BL21(DE3) One Shot® chemically competent *E. coli* were transformed by heat shock [66] with the pET-SUMO-Httex1-23Q plasmid containing a single mutation in the *HTTEX1* (at position A2C or A82C) or a double mutation (positions A2C and A82C). The cells were plated on LB-Agar plates supplemented with Km (50 µg/mL) and incubated overnight at 37 ºC. An isolated colony was then inoculated in LB-Km medium and left to grow overnight at 37 ºC with 250 rpm shaking. Next morning, 10 mL of the overnight culture was inoculated in a fresh 90 mL LB-Km medium, which was further grown for

approximately 4 hours at 37 ºC, 250 rpm. To scale-up the culture, 1 L LB-Km medium was inoculated with the previous culture for obtaining an optical density at 600 nm (OD_{600}) of 0.1. The cells were then grown at 37 ºC, 250 rpm until they reached an OD_{600} of 0.4-0.8. At this stage, the protein expression was induced with 0.6 mM IPTG, and the culture was left incubating overnight at 16 ºC, 180 rpm. The cells were then collected by centrifugation at 8000 rpm for 10 minutes at 4 ºC and resuspended in 60 mL buffer A (50 mM Tris-HCl, pH 8.0, 500 mM NaCl, 15 mM Imidazole) supplemented with 0.1 mM PMSF and 1 tablet of cOmplete Mini EDTA-free Protease Inhibitor Cocktail. Finally, the cells were stored at -80 ºC until the purification steps.

2.2.2 Purification of the tag-free Httex1-23Q

Cells were initially sonicated (Branson Sonifier 250) on ice with 9 cycles of 15 pulses (50% duty cycle and an output of 9) and 5 minutes of rest between cycles. The cell lysate was then cleared by centrifugation at 17,600 x *g* for 1 hour at 4 ºC. The supernatant was collected and filtered with 0.44-µm syringe filters (low protein binding) to remove leftover cell debris.

A first Immobilized Metal Affinity Chromatography (IMAC) was performed to purify the His_6-SUMO-Httex1-23Q mutated fusion protein in an ÄKTA Start System (GE Healthcare). Briefly, the filtrated lysate was loaded into a 5-mL HisTrap FF column previously equilibrated with buffer A and with a flow rate of 1.5 mL/min. Non-specific bound proteins were washed out with 10 column volumes (CV) of buffer A at a flow rate of 5 mL/min. The fusion protein was then eluted with a gradient of 5–100% of buffer B (50 mM Tris-HCl, pH 8.0, 500 mM NaCl, 500 mM Imidazole) at a flow rate of 1.5 mL/min and in 5-mL fractions.

The fractions with the His_6-SUMO-Httex1-23Q mutated fusion protein were joined, concentrated to about 10 mL and the buffer was exchanged to buffer C (50 mM Tris-HCl, pH 8.0, 150 mM NaCl, 15 mM Imidazole) using an Amicon® Ultra-15 with 10 kDa cutoff. To remove the His_6-SUMO tag, the concentrated fraction was incubated with ubiquitin-like-specific protease 1 containing a His_6-tag (His_6-Ulp1) (1:50) and 1 mM DTT at 4 ºC for 3 hours in a rotator.

A second IMAC was then carried out to purify the tag-free HTT-23Q protein from the protease and the His_6-SUMO tag. Here, the sample was loaded into the 5-mL HisTrap FF column equilibrated with buffer C, and the tag-free protein was eluted in the flow-through at flow rate of 1.5 mL/min and in 2.5 mL fractions.

The fractions containing the tag-free Httex1-23Q mutated protein were buffer exchanged to buffer SEC (50 mM Tris-HCl, pH 8.0, 200 mM NaCl) with 5 mM DTT and finally concentrated to around 500 µL in an Amicon® Ultra-15 with 3 kDa cutoff. Lastly, a Size Exclusion Chromatography (SEC) was performed to final purification using a Superdex 75 10/300 GL column equilibrated with buffer SEC at a flow rate of 0.3 mL/min and fractions of 0.5 mL were collected.

2.2.3 Single-labeling of Httex1-23Q-A2C or A82C with Acrylodan or Atto 488 maleimide

About 500–800 µL of freshly purified Httex1-23Q protein with a mutation at position A2C or A82C (concentrations higher than 100 µM) was initially incubated with 1 mM of DTT for 30 minutes at

room temperature (RT). The protein was then loaded into two coupled 5 mL-HiTrap desalting columns previously equilibrated with the labeling buffer (20 mM Tris, pH 7.4, 50 mM NaCl, 6 M guanidine hydrochloride). Fractions of 0.5 mL were collected and analyzed by SDS-PAGE.

The protein was then incubated with the fluorescent probe (at a ratio of protein:dye of 1:10): (i) Acrylodan for 4 hours at RT and (ii) Atto 488 maleimide overnight at 4 ºC, both under continued stirring on an amber glass vial protected from light. To purify the labeled Httex1-23Q protein from the free dye, the sample was loaded into the desalting columns now equilibrated with the buffer SEC. Fractions of 0.5 mL were again collected and analyzed by SDS-PAGE.

The fractions containing the protein were further analyzed to determine: (i) the dye concentration by measuring absorbance at 360 nm for Acrylodan ($\varepsilon_{Acrylodan}$ = 12,900 M^{-1} cm^{-1} in water) [67] or at 500 nm for Atto 488 maleimide ($\varepsilon_{Atto488}$ = 90,000 M^{-1} cm^{-1} in Phosphate Buffered Saline, pH 7.4) [68]; and (ii) the protein concentration. We used the Modified Lowry Protein Assay Kit [69], or the BCA Protein Assay Kit [70] for protein quantification with similar results. The protein was then aliquoted in 20 µL fractions, flash-frozen in liquid nitrogen and finally stored at -80 ºC until further use.

2.2.4 Double-labeling of Httex1-23Q-A2C/A82C with Alexa 488 and 594 maleimide

The protocol employed for double-labeling Httex1-23Q – creating the smFRET construct with donor (Alexa 488) and acceptor (Alexa 594) fluorophores – was similar to the previously described for single-labeling (section 2.2.3) with minor modifications. Here, Httex1-23Q-A2C/A82C was initially incubated with Alexa 488 maleimide (donor fluorophore) in a molar ratio of 0.5:1 (dye:protein) during 2 hours at RT with constant stirring and protected from light. Afterwards, Alexa 594 maleimide (the acceptor fluorophore) was added at 5x in molar excess and further left incubating overnight at 4 ºC with stirring and protected from light. This protocol results in different combinations of donor and acceptor fluorophores on the labeling positions (as Httex1-23Q has two cysteines and multiple combinations for labeling with Alexa 488 and 594).

The double-labeled Httex1-23Q protein was then purified from the unreacted donor and acceptor dyes as described before (section 2.2.3). The fractions collected were also analyzed by absorption spectroscopy to confirm the presence of donor and acceptor fluorophores. The labeled protein was then aliquoted in 20 µL fractions, which were also flash-frozen in liquid nitrogen and stored at -80 ºC until further use.

2.3 SDS-PAGE

The Httex1-23Q fragment has an estimated very low absorption extinction coefficient at 280 nm since it does not contain any tryptophan. Therefore, during the expression, purification and labeling, several SDS-PAGE gels were performed to identify the fusion protein and the tag-free Httex1-23Q protein. The gels were prepared with a 5% stacking gel and a resolution gel of 15% in polyacrylamide. The NZYColour Protein Marker II with a scale of 11 to 245 kDa was used in all gels as reference. The samples were prepared with a loading buffer (50 mM Tris-HCl, pH 6.8, 100 mM DTT, 2% SDS, 0.1% bromophenol blue, and 10% glycerol) (20 µL of sample + 10 µL of loading buffer) and incubated at 100

ºC for 5 min. At first, electrophoresis ran at 90 V for 10 minutes and then at 175 V for 40-50 minutes in the Mini-PROTEAN Tetra Cell (Bio-Rad). BlueSafe was used to stain the gels.

2.4 Preparation of large unilamellar vesicles

In this work, large unilamellar vesicles (LUVs) of distinct lipid compositions were prepared: (i) pure POPC; (ii) 25:75 POPC:POPS; and (iii) a 1:1:1 SM:Chol:POPC ternary mixture for mimicking lipid rafts (molar ratio) [71]. Briefly, the stock solutions of lipids were combined in appropriate amounts for a final lipid concentration of 2–5 mM. First, the organic solvent (chloroform) was evaporated using a stream of nitrogen, and then under vacuum for at least 2 hours. The dry lipid film was resuspended in a 50 mM HEPES, pH 7.4, 50 mM NaCl buffer (previously filtered). Next, ten freeze-thaw cycles were performed to re-equilibrate the suspension and to obtain multilamellar vesicles (MLVs). Finally, the resulting suspension was extruded (31 times) through a 50-nm pore diameter polycarbonate membrane in an Avanti Mini-Extruder system to produce LUVs. This procedure was performed at a temperature above the melting temperature of the lipid mixtures. The vesicle diameter and the polydispersity index were confirmed by Dynamic Light Scattering.

2.5 Fluorescence spectroscopy

2.5.1 Steady-state fluorescence measurements

Steady-state fluorescence experiments were performed in a Horiba Jobin Yvon Fluorolog 3-22 spectrofluorometer using double monochromators in the excitation/emission and in right angle geometry. The measurements were conducted in 5 x 5 mm quartz cuvettes (Helma Analytics) at RT.

Samples were prepared with a constant protein concentration of 0.6 µM or 50 nM when the fluorescent probe was Acrylodan or Atto 488, respectively, and a variable lipid concentration, ranging from 0 to 1 mM of LUVs. The dilutions to obtain the final concentration of protein were done with a buffer containing 50 mM HEPES, pH 7.4, 50 mM NaCl which was also the buffer used as a blank. The lipid-protein mixtures were prepared on the day of the fluorescent measurements. The emission spectra were recorded with excitation at 370 nm and 480 nm, for the Httex1-23Q constructs labeled with Acrylodan and Atto 488, respectively. The fluorescence spectral center-of-mass, $\langle\lambda\rangle$, was calculated from the emission spectra, as [72]:

$$\langle\lambda\rangle = \frac{\sum_i I_i \cdot \lambda_i}{\sum_i I_i} \quad (1)$$

where I_i is the fluorescence intensity recorded at the corresponding wavelength λ_i.

For the steady-state fluorescence anisotropy experiments, samples were excited as described before and the polarized emission was detected at the maximum emission wavelength in solution and for the membrane-bound state: (i) for Httex1-23Q labeled with Atto 488 (for both A2C and A82C) was fixed at 520 nm; (ii) for Httex1-23Q-A82C-Acrylodan was recorded exclusively at 525 nm; and finally (iii)

for Httex1-23Q-A2C-Acrylodan was detected at 525 nm for solution and at 495 nm for samples with lipid. The fluorescence anisotropy, $\langle r \rangle$, was calculated as:

$$\langle r \rangle = \frac{I_{VV} - G \cdot I_{VH}}{I_{VV} + 2 \cdot G \cdot I_{VH}} \quad (2)$$

with I_{VV} and I_{VH} being the vertical and horizontal components of the polarized fluorescence emission, when the sample is excited with a vertical polarized light, respectively. The G factor is given by the I_{HV}/I_{HH} ratio (which are the components with horizontal excitation) and allows correction for the transmission efficiency of the monochromator to the polarization light. Blanks were always prepared (buffer and lipid), and their data were subtracted to the respective sample. For anisotropy, at least five measurements for each sample were performed, and the data are displayed as a mean with the respective standard deviation.

2.5.2 Time-resolved fluorescence measurements

Time-resolved fluorescence intensity and anisotropy experiments were performed by the time-correlated single-photon timing technique using a step-up previously described [73]–[75]. The setup holds a Jobin-Yvon HR320 monochromator with a cutoff filter and a Hamamatsu R-2809U microchannel plate photomultiplier. Here, we measured the samples previously characterized by steady-state fluorescence (section 2.5.1). The Httex1-23Q labeled with Acrylodan was excited at 340 nm (with a frequency doubled secondary cavity-dumped dye laser of DCM-Coherent 701-2) and labeled with Atto 488 at 480 nm (with a BDS-SM-488FBE pulsed picosecond diode laser from Backer & Hickl). The emission was recorded as described above for steady-state fluorescence anisotropy. The fluorescence intensity decays ($I(t)$) were acquired placing the emission polarizer at the magic angle (54.7º) relative to the vertically polarized excitation beam. For the fluorescence anisotropy decays, the parallel (I_{VV}) and perpendicular (I_{VH}) emission polarized components of the fluorescence were alternatively collected. The instrument response function (IRF) was recorded as excitation light scattered by a Ludox solution (silica, colloidal water solution, Aldrich). Fluorescence intensity decays were acquired in 1024 channels.

Fluorescence decay analysis

Fluorescence decay analysis were carried out in TRFA Data Processing Package version 1.4 (developed by the Department of System Analysis and Computer Modelling from Belarusian State University). The goodness of the fits was evaluated from the χ^2 value (<1.3) and a random distribution of weighted residuals and autocorrelation plots.

The florescence intensity decays were analyzed assuming a sum of discrete exponential terms [76]:

$$I(t) = \sum_{i=1}^{n} \alpha_i \exp\left(-\frac{t}{\tau_i}\right) \quad (3)$$

in which α_i and τ_i are the amplitude and the lifetime of the i^{th} decay component of fluorescence, respectively [73], [76]. The amplitude-weighted mean fluorescence lifetime is given by [76]:

$$\langle \tau \rangle = \sum_i a_i \tau_i \tag{4}$$

The fluorescence anisotropy decays, $r(t)$, were analyzed by global fitting of $I_{VV}(t)$ and $I_{VH}(t)$ considering that:

$$I_{VV}(t) = \frac{1}{3} I(t)[1 + 2 \cdot r(t)] \tag{5}$$

$$I_{VH}(t) = \frac{1}{3} I(t)[1 - r(t)] \tag{6}$$

where $r(t)$ is also described by a sum of discrete exponential terms [75], [76]:

$$r(t) = \sum_{i=1}^{n} \beta_i \exp\left(-\frac{t}{\phi_i}\right) \tag{7}$$

here, β_i and ϕ_i represent the normalized amplitude and the rotational correlation time of the i^{th} anisotropy decay component, respectively [73], [76]. The global analysis was constrained by the experimental steady-state fluorescence anisotropy, $\langle r \rangle$, by introducing a G factor calculated as [75]:

$$G = \frac{(1 - \langle r \rangle)}{1 + 2 \cdot \langle r \rangle} \left(\frac{\int I_{VV}(t)\, dt}{\int I_{VH}(t)\, dt} \right) \tag{8}$$

The G factor accounts for experimental artifacts, such as photobleaching of the probes and laser fluctuations during the measurements (the calculated values were always close to 1) [75].

2.5.3 Single-molecule FRET measurements

2.5.3.1 Theoretical background

Förster resonance energy transfer (FRET) is a nonradiative energy transfer between a donor fluorophore to an acceptor fluorophore (due to dipole-dipole coupling). In the last couple of decades, FRET has become widely used in biology and biochemistry fields as a spectroscopic ruler to determine distances in biomolecules and intramolecular assemblies at nanometer scale, since the efficiency of transfer, ET_{eff}, depends on the inverse of the sixth power of the donor-acceptor distance.

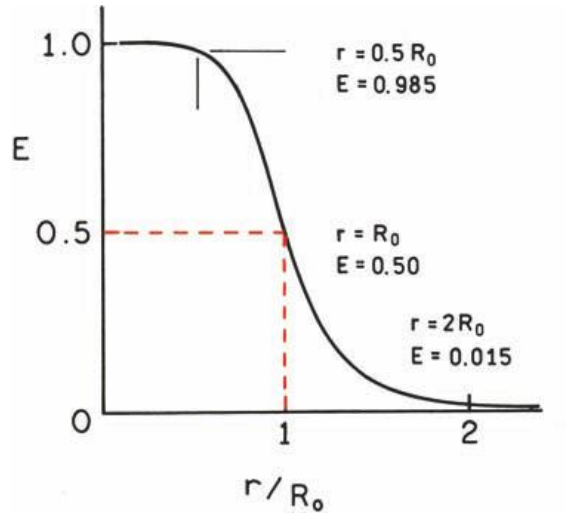

Figure 2.3 – Dependence of the energy transfer efficiency on distance. In this figure, *E* is the FRET efficiency, *r* is the donor-acceptor distance and R_0 is the Förster distance. Reproduced from [76].

In particular, single-molecule FRET (smFRET) measures FRET at single donor-acceptor pair (at single molecule level). smFRET has already been used in many fields to rapidly answer fundamental questions: the quantification and characterization of binding events; protein folding and conformational changes; motor proteins; RNA folding and catalysis; DNA conformational changes; vesicle fusion; ion channels; and signal transduction [77]. Specifically, when the donor and acceptor are located at the same molecule, valuable information can be obtained: (i) the efficiency of energy transfer between the donor and acceptor is highly sensitive to the distance between them, which makes smFRET an excellent tool for measuring changes in molecular distance or conformational changes; (ii) if the donor and acceptor are attached to different parts of the molecule, changes in FRET efficiency can provide information about the interactions between the different parts of the molecule, such as the binding of ligands or the formation of protein complexes; and (iii) FRET can also be used to study the flexibility and dynamics of a molecule, by measuring the changes in FRET efficiency over time. This can provide information about the conformational changes and structural fluctuations that occur during protein folding, enzyme catalysis, or other biological processes [77], [78].

The two most common setups used for smFRET measurements are the confocal microscope (freely diffusing molecules in solution, here used) and the total internal reflection fluorescence (TIRF) microscope (surface-immobilized molecules).

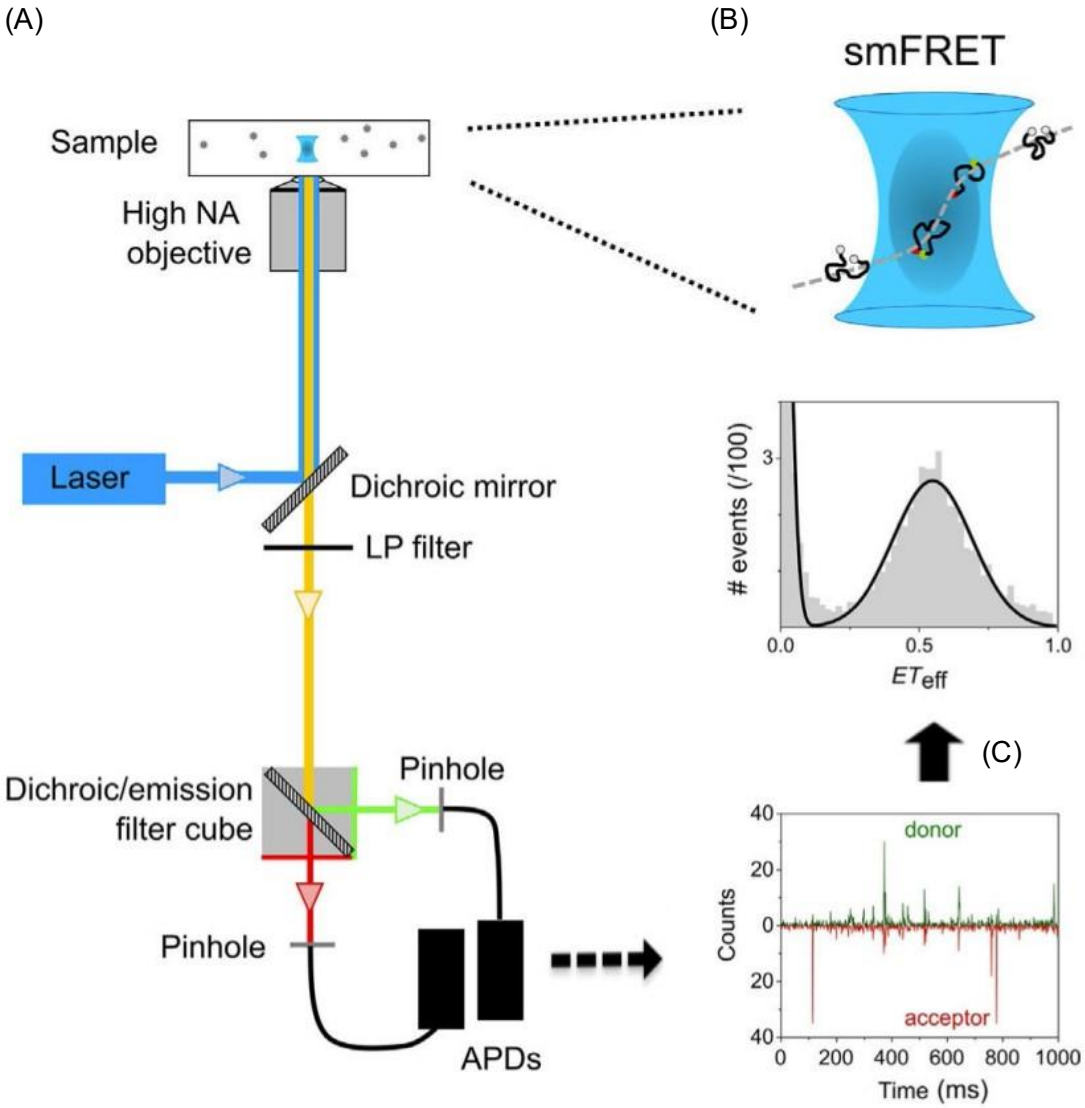

Figure 2.4 – Overview of smFRET instrument and measurements using a confocal setup. In a typical confocal setup (A) the laser beam is focused by a high numerical aperture (NA) objective lens to a diffraction-limited confocal remove the excitation light. It finally passes through a long-pass filter and is focused into the confocal pinhole. Each donor-acceptor-labeled molecule emits a burst of photons during smFRET measurements as it diffuses through the confocal volume (B). Afterwards, (C) the ET_{eff} values for every photon burst are calculated and plotted as a histogram. Replicated and adapted from [64].

2.5.3.2 Setup description

Our home-built system is based on a confocal setup for measuring freely diffusing molecules in solution and with an intensity-based for detecting simultaneously donor and acceptor photon counts to further determine ET_{eff}. Our system uses a manual Olympus IX-73 two-deck microscope as a frame, containing an objective UPLSAPO 60x/1.2NA water immersion (Olympus) and two avalanche photodiode detectors (APDs) with higher sensitivity for detecting single photons. We also use a 488-nm continuous laser (Sapphire 488-50 CW, Coherent) for directly exciting donor fluorophores. Briefly, the laser is focused on the back aperture of the objective and the fluorescence emission is collected by the same objective (inverted microscope). Afterwards, the fluorescence is: (1) split from the excitation light using

a dichroic mirror (ZT488rdc dichroic with a long pass ET500lp filter from Chroma), (2) directed for the left microscope port coupled to a U-DPCAD dual port unit (Olympus) containing the FRET cube (ZT561rdc dichroic in combination with ET525/50m and AT600lp filters for donor and acceptor detection, respectively, from Chroma), and finally (3) focused into 100-µm diameter optical fibers (OzOptics) for achieving the confocal aperture. Both fibers were coupled to APDs (SPCM-AQRH-14-FC from Excelitas), and the signal output was recorded using digital correlators (Flex03LQ-12; correlator.com).

2.5.3.3 Preparation of double-stranded DNA

Complementary oligonucleotides labeled with A488 or A594 were hybridized for creating double-stranded DNA with 10-bases between each fluorophore (10-mer DNA standard). Briefly, both oligonucleotides were initially dissolved in water for a final concentration of 250 µM. In an Eppendorf tube protected from light, the oligonucleotides were mixed in 100 µL of oligo hybridization buffer (10 mM Tris-HCl, pH 8, 15 mM $MgCl_2$, 100 mM NaCl) for obtaining 2 µM for each oligonucleotide. For setting the hybridization conditions, 1 L of water was initially boiled in a hot plate with stirring and then the heat/stirring were turned off. Immediately, the sample was incubated there and left overnight. The 10-mer DNA was then aliquoted in 10 µL fractions and stored at -20 ºC.

2.5.3.4 System calibrations

The optical pathway/setup were previously built by the supervisor and the calibrations for smFRET were performed in the scope of this thesis. The system was built in a floating optical table and in a dark room, with temperature/humidity controlled for improving the stability. Here, we performed as described below: (i) the determination of the Z-position of the optical fibers, (ii) calibrations of the confocal volume and bleed-through of donor emission in the acceptor channel, and (iii) finally measure a FRET standard (10-mer DNA).

Z-position of the optical fibers

The optical fibers are connected to the U-DPCAD dual port unit, and the X/Y-positions are controlled by a XY Translator with Micrometer Drive (Thorlabs). The Z-position was adjusted manually and calibrated by fluorescence correlation spectroscopy (FCS) measurements. Briefly, for each Z-position, FCS curves were acquired for 10 nM of Rhodamine 110 in water (10 curves for 10 seconds). The curves were analyzed by:

$$G(\tau) = \frac{1}{N} \cdot \frac{1}{1 + \frac{\tau}{\tau_D}} \cdot \sqrt{\frac{1}{1 + \frac{s^2 \tau}{\tau_D}}} \tag{9}$$

Determination of the confocal volume and bleed-through of the donor fluorescence into the acceptor channel (β-factor)

The confocal volume (*s*-factor) was determined by FCS measurements of 10 nM Alexa 488 in water. The curves were analyzed as described above (Equation 9) to determine *s*. Simultaneously, we

recorded the intensities in both donor and acceptor channels for Alexa 488 (with the FRET cube in the pathway). The β-factor is given by the ratio of intensities measured in the acceptor channel regarding the donor channel.

Determine the ET_{eff} for 10-mer dsDNA

The previously prepared 10-mer dsDNA (in 2.5.3.3) was diluted in 20 mM Tris-HCl, pH 7.4, 50 mM NaCl. The dilution should be in a way that the final concentration of 10-mer dsDNA allows for a suitable reading by the detectors (typically between 10-100 nM). Ten minutes measurements were performed to establish the ET_{eff} for 10-mer ds DNA. Deviations of the obtained ET_{eff} with an expected histogram could indicate that there was issue with the system, or the reagents used.

2.5.3.5 smFRET data analysis

Data collected by the Correlator were analyzed using lab-written MATLAB scripts. Briefly, these data correspond to the number of photons detected in each channel in 1-ms time bin. We then applied a threshold to distinguish the counts coming from the labeled sample from the background. Typically, a threshold of ~30 photons gives zero FRET events for the buffers [64], [79]. Next, the efficiency of transfer, ET_{eff}, was calculated for each photon burst according to:

$$ET_{eff} = \frac{I_a - \beta I_d}{(I_a - \beta I_d) + \gamma(I_d + \beta I_d)} \tag{10}$$

where I_a and I_d are the fluorescence intensities collected in the acceptor and donor detectors, respectively. β-factor accounts for bleed-through of the donor fluorescence into the acceptor channel, while γ corrects for the difference in the donor (η_d) and acceptor (η_a) detection efficiency, and also quantum yield for donor (ϕ_d) and acceptor (ϕ_a) fluorophores [64], [80]:

$$\gamma = \frac{\eta_a \phi_a}{\eta_d \phi_d} \tag{11}$$

The ET_{eff} calculated are then plotted as a histogram, which contains a peak with a mean $ET_{eff} = 0$, caused by molecules with photobleached, absent or nonfluorescent acceptor dyes (donor-only labeled). The histograms were then fitted with a multipeak Gaussian function to account for the zero peak and for donor-acceptor-labelled sample, using the lab-written MATLAB scripts. The number of events as a function of time was also tracked to monitor sample concentration over time.

3 Results and discussion

3.1 Production of single- and double-labeled Httex1-23Q constructs

The Httex1-23Q production was previously optimized in the host lab. Briefly, Httex1-23Q was expressed in *E. coli* BL21 (DE3) as a fusion protein – containing a His_6-SUMO tag at the N-terminal – at 16 ºC and with 0.6 mM IPTG. Httex1-23Q was engineered to introduce a single-cysteine (position A2C or A82C) for labeling with Acrylodan or Atto 488 maleimide or two-cysteines (positions A2C and A82C) for labeling with Alexa 488 and 594 maleimide (donor and acceptor fluorophores for smFRET, respectively).

The purification of tag-free Httex1-23Q comprised several steps: (1) a first IMAC was performed to purify the mutated His_6-SUMO-Httex1-23Q fusion protein from the cell lysate; (2) the His_6-SUMO tag was cleaved by His_6-Ulp1 protease; (3) a second IMAC was conducted to purify the tag-free Httex1-23Q from the His_6-SUMO tag, the fusion protein and the protease; and finally (4) a SEC was performed for final purification of the tag-free Httex1-23Q. The typical SDS-PAGE gels obtained during the Httex1-23Q purification are shown in Figure 3.1. We obtained similar results for the different Httex1-23Q constructs and highly pure protein. Since we adopted the same strategy for all constructs, here we only show the results for Httex1-23Q-A82C construct labeled with Acrylodan to simplify the reading of this thesis.

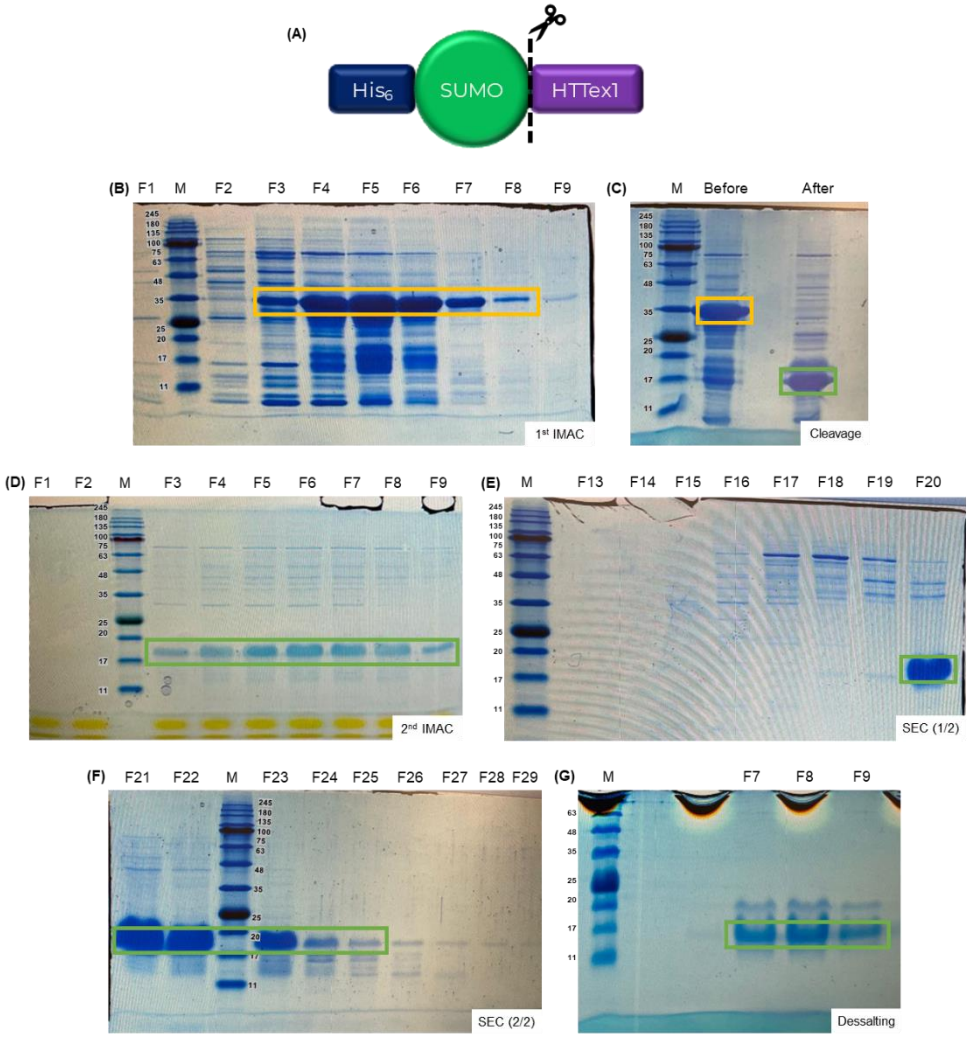

Figure 3.1 – Purification steps of Httex1-23Q-A82C and labeling with Acrylodan monitored by SDS-PAGE. (A) Schematic representation of His_6-SUMO-Httex1-23Q fusion protein: His_6-tag is shown in blue; SUMO-tag in green; and the Httex1-23Q in purple. The black line represents the cleavage location targeted by the His_6-Ulp1. After cleavage, tag-free Httex1-23Q is produced without any leftover amino acid residues from the His_6-SUMO tag. (B) The His_6-SUMO-Httex1-23Q-A82C fusion protein was initially purified by IMAC. The highlighted fractions (F3 to F8) indicate the fusion protein. (C) The His_6-SUMO tag was cleaved by a SUMO protease (His_6-Ulp1). The band corresponding to the His_6-SUMO-Httex1-23Q-A82C fusion protein (yellow box) disappeared after the cleavage and a new band appeared at a lower MW (highlighted by the green box). (D) During the second IMAC, the Httex1-23Q-A82C was purified from the His_6-SUMO tag and His_6-Ulp1 protease. The tag-free protein was eluted in the flow-through (F3 to F9). (E-F) A SEC was performed for final purification. The fractions containing pure tag-free Httex1-23Q protein (F20 to F22) were labeled with Acrylodan. (G) The unreacted free dye was removed from the labeled protein by desalting columns.

Both the His_6-SUMO-Httex1-23Q fusion protein and the tag-free Httex1-23Q protein run at high molecular weights (MW) in the SDS-PAGE gel due to the high proline content and their intrinsically disordered features [59], [81]. The fusion protein has 23 kDa (calculated using the Expasy – Compute pI/Mw tool [82]), and runs around the 35 kDa marker in the SDS-PAGE gel; and the tag-free Httex1-23Q protein has a theoretical MW of 9.94 kDa but it runs at 17–20 kDa as previously reported [59], [81].

For the first IMAC, the His_6-SUMO-Httex1-23Q bound to the nickel-column (HisTrap FF) during the loading step and unbound proteins were washout with buffer A (containing a low imidazole

concentration). Afterwards, using a gradient (5–100%) with the imidazole-rich buffer (buffer B), the fusion protein was eluted and collected in 5mL-fractions, namely in fractions F3 to F8 (Figure 3.1(B)). At this purification step, the His_6-SUMO-Httex1-23Q fusion protein was still not pure since other proteins initially bound to the nickel-column and were co-eluted during the gradient with buffer B.

The fractions containing the fusion protein were exchanged to buffer C (low salt and imidazole concentration) and concentrated to ~12 mL. The His_6-SUMO tag cleavage with the His_6-Ulp1 protease was highly efficient (Figure 3.1(C)), as the band of the fusion protein (running around the 35 kDa marker in the SDS-PAGE gel) disappeared and instead two new intense bands appeared in the region between 17–20 kDa markers.

In the second IMAC, the tag-free Httex1-23Q protein was collected in the flow-through and both the His_6-SUMO tag and the His_6-Ulp1 protease were retained in the nickel-column. Figure 3.1(D) shows the fractions containing the tag-free protein (F3–F9). These fractions were pooled and concentrated (while also performing a buffer exchange to buffer SEC) for a final purification by SEC. In this step, the tag-free protein was purified based on its size, being eluted in the fractions F20 to F22 (Figure 3.1(E-F)).

Finally, the labeling with the fluorescent probes, here exemplified with Acrylodan (Figure 3.1(G)), also occurred as expected. First, we used two coupled 5-mL HiTrap desalting columns (as mentioned in sections 2.2.3 and 2.2.4) to remove DTT (quencher of the labeling reaction) and also perform a buffer exchange to the labeling buffer. The protein was collected, and the selected fractions (F7 to F9) were tested on a SDS-PAGE gel to confirm the presence of the protein. For single labeling, the selected fractions were incubated with Acrylodan or Atto 488 for 4 hours or overnight, respectively. For double-labeling, the fractions were initially incubated with Alexa 488 for 2 hours and later with Alexa 594 overnight. After the incubation, the single- or double-labeled sample was loaded again into the HiTrap desalting columns to separate the protein from the unreacted dye (while also performing a buffer exchange to remove guanidine hydrochloride). The labeled protein was collected in 0.5 mL fractions and analyzed by SDS-PAGE (Figure 3.1(G)) and UV-Vis.

The dye was quantified by absorbance and using the respective extinction coefficient of each probe. In addition, we used the BCA or Lowry methods for protein quantification, obtaining typical protein concentrations about 15 – 25 µM (depending on the fraction).

3.2 Fluorescence properties of the single-labeled Httex1-23Q-A2C and -A82C-Acrylodan

This thesis aimed to evaluate the effects of distinct membrane compositions on Httex1-23Q lipid interaction. Initially, we characterized the binding of Httex1-23Q single-labeled with Acrylodan at both flanking regions – A2C at N17 and A82C at PRR – with LUVs prepared with variable lipid content. Here, we used Acrylodan, a thiol-reactive probe, to report on local polarity. The Acrylodan fluorescent probe is a thiol reactive probe that forms a very strong bond. This probe is also sensitive to the polarity of the solvent, in both fluorescent intensity and emission wavelength, which are dependent on the dielectric constant of the environment that surrounds the probe (solvent), and also on the environment viscosity, since dipole reorientation via rotational diffusion is required [83]. This property is called solvent relaxation

and it originates the Stokes shift (Figure 3.2) [76]. This shift is the wavelength difference observed between the maximum wavelength of the absorption and emission spectrum for the same electronic transition. The bigger the polarity of the solvent, there is a higher solvent relaxation that causes a larger loss of energy, meaning there is a deviation of the spectra to higher wavelengths (red shift). The opposite is also true: if the solvent polarity decreases, there is less solvent relaxation and less loss of energy, and the shift goes to lower wavelengths (blue shift).

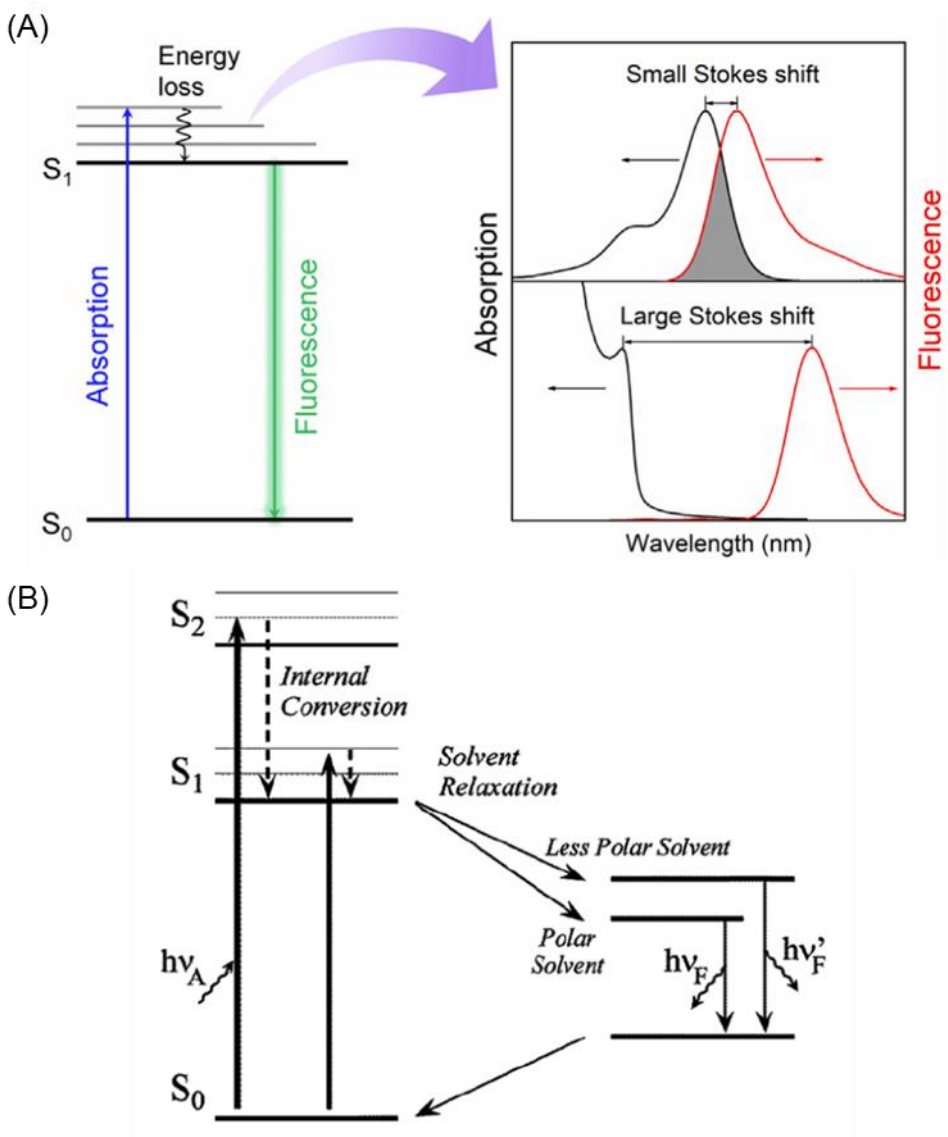

Figure 3.2 – Stokes shift generation described by the Jablonski diagram for fluorescence. (A) When a fluorophore absorbs light, it is pushed from the ground state of energy (S_0) to a higher excited energy state, quickly relaxing to the first excited energy level (S_1) which then decays to the ground state. The loss of excitation energy during this process results in a higher wavelength of emission (when compared to the absorption), originating the Stokes shift. Reproduced from [84]. (B) Jablonski diagram illustrating fluorescence with solvent relaxation, the origin of the Stokes shift. Reproduced from [85].

Httex1-23Q does not contain any cysteine in its amino acid chains composition. To successfully label the protein with the fluorescent probes, a mutagenesis consisting of a single amino acid

substitution was performed, replacing an alanine for a cysteine (that contains a thiol group) in two positions within Httex1-23Q (A2C or A82C), which correspond to the N- (Nt17) and C-terminal domain, respectively. The absence of naturally occurring cysteines on Httex1 allows for a specific labeling on the desired location. The fluorescence properties of Acrylodan coupled to both regions were characterized through steady-state and time-resolved fluorescence measurements.

Figure 3.3 shows the fluorescence emission spectra of both Acrylodan-labeled Httex1-23Q-A2C and A82C constructs in aqueous solution and with increasing lipid concentrations. We used LUVs composed of three different lipid mixtures: pure POPC, 1:1:1 SM:Chol:POPC and 25:75 POPC:POPS. The corresponding parameters obtained from the fluorescence emission spectra, including $\langle\lambda\rangle$ and the normalized integrated area of the respective spectra, are presented in Figure 3.4(A-B and C-D, respectively). Additionally, the changes in $\langle r\rangle$ and $\langle\tau\rangle$ are also displayed in Figure 3.4(E-F) and Figure 3.5, respectively. The fluorescence parameters obtained for both constructs in solution and with 1 mM LUVs are shown in Table 3.1.

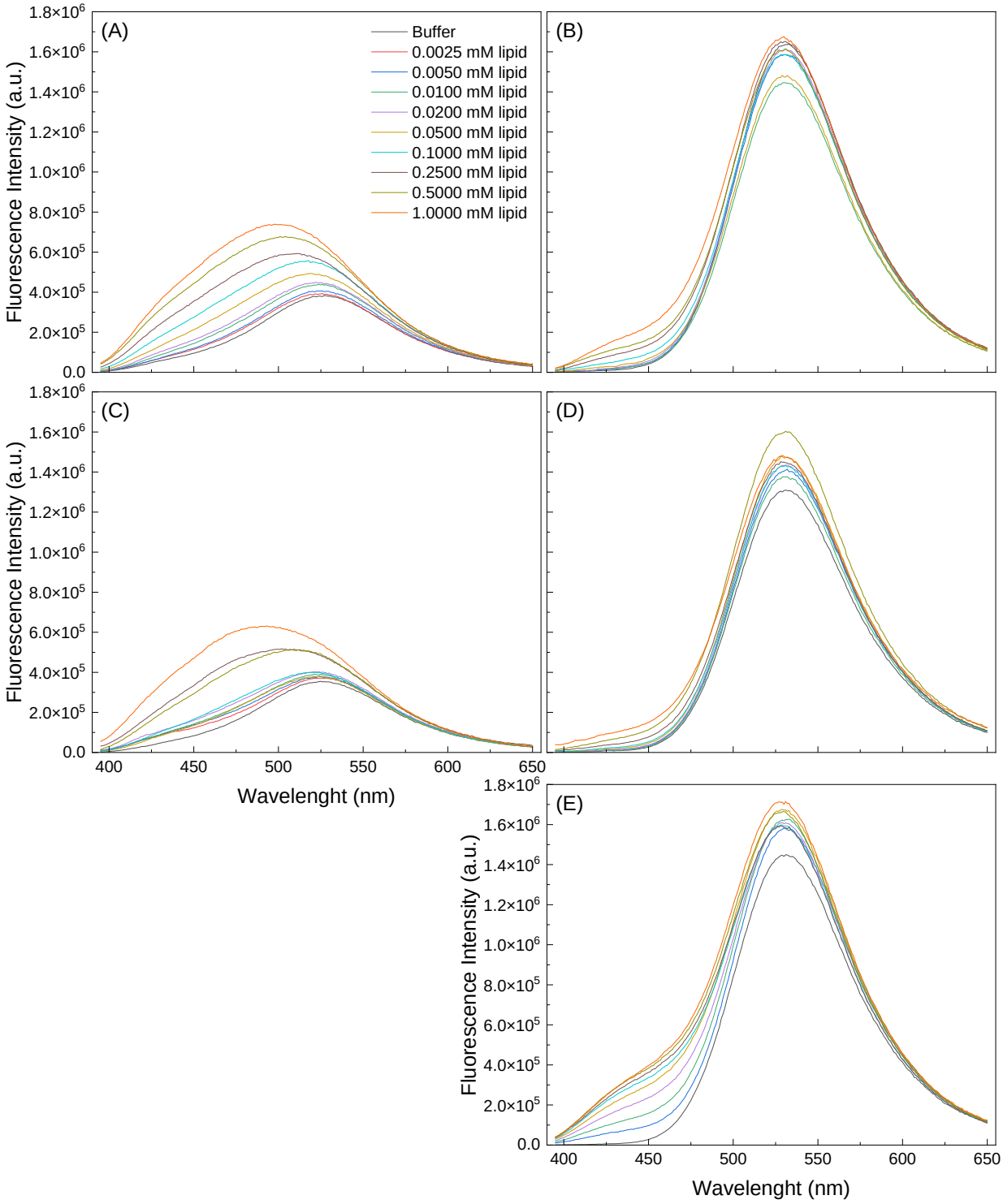

Figure 3.3 – Fluorescence emission spectra of (A and C) Httex1-23Q-A2C-Acrylodan and (B, D and E) Httex1-23Q-A82C-Acrylodan in solution (buffer) and with increasing lipid concentration. LUVs composed of (A-B) POPC, (C-D) 1:1:1 SM:Chol:POPC and (E) 25:75 POPC:POPS were used. The protein concentration for all samples was of 0.6 µM and measurements were performed in a 50 mM HEPES, pH 7.4, 50 mM NaCl buffer at RT. The excitation and emission slits were both opened at 5 nm for Httex1-23Q-A2C and at 4 nm for Httex1-23Q-A82C.

3.2.1 Characterization of Httex1-23Q-A2C and -A82C-Acrylodan in solution

As previously mentioned, Acrylodan is a highly sensitive fluorescent probe that is affected by the polarity of the surrounding environment. The fluorescent properties of Acrylodan (Figure 3.4 and Table 3.1) located at the Nt17 domain (Httex1-23Q-A2C construct: λ max = 524 nm, $\langle\lambda\rangle$ = 527 nm, $\langle r\rangle$ = 0.12 and $\langle\tau\rangle$ = 0.95 ns) were slightly different from those observed at the PRR (Httex1-23Q-A82C construct: λ max = 532 nm, $\langle\lambda\rangle$ = 543 nm, $\langle r\rangle$ = 0.12 and $\langle\tau\rangle$ = 1.31 ns). The λ max observed for the A82C-labeled construct in solution is typical of disordered regions as previously reported, where it has been shown to be around 530 nm [86]. Nevertheless, the λ max observed for Httex1-23Q-A2C showed a slight blue-shift from the values of the Httex1-23Q-A82C construct. This is an indication that the Nt17 domain, when in solution, may exhibit transient secondary structures or a more collapsed conformation. It could partially shield the Acrylodan probe from the surrounding solvent (which in this study is mostly water, highly polar) and therefore decrease the local polarity experienced by Acrylodan. This is a plausible explanation for the slight decrease of λ max and the observed differences for the other parameters as well.

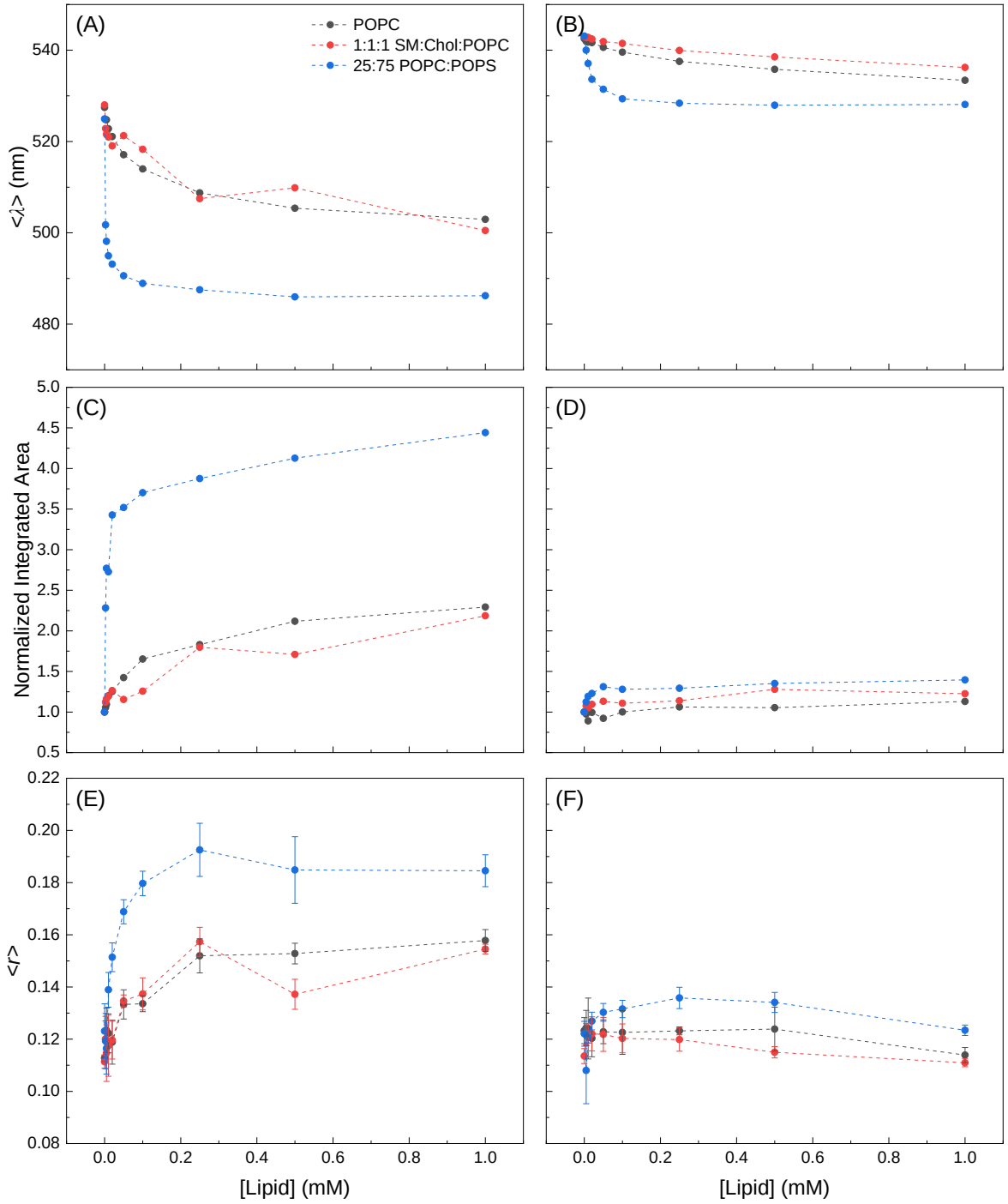

Figure 3.4 – Fluorescence properties of the (A, C and E) Httex1-23Q-A2C-Acrylodan and (B, D and F) Httex1-23Q-A82C-Acrylodan-labeled constructs. Variations of (A-B) $\langle\lambda\rangle$, (C-D) normalized integrated area of the fluorescence emission spectra and (E-F) $\langle r\rangle$ with the lipid concentration. LUVs composed of POPC (black), 1:1:1 SM:Chol:POPC (red) and 25:75 POPC:POPS (blue) were used. The samples had a protein concentration of 0.6 μM and were in a 50 mM HEPES, pH 7.4, 50 mM NaCl buffer at RT. For steady-state fluorescence anisotropy, 10 nm slits in both the excitation and emission were used for Httex1-23Q-A2C-Acrylodan, while for the Httex1-23Q-A82C-Acrylodan was employed 5 nm and 8 nm for the entrance and exit slits, respectively. Results for the Httex1-23Q-A2C-Acrylodan construct with LUVs 25:75 POPC:POPS were obtained by Dr. Tânia Sousa. They are shown here to compare with the results from this work. Dashed lines were drawn as guides to the eye.

Table 3.1 – Fluorescence parameters obtained for Httex1-23Q-A2C and A82C-Acrylodan-labeled in buffer (solution) and with 1 mM LUVs (POPC, 1:1:1 SM:Chol:POPC and 25:75 POPC:POPS). The data was acquired with protein concentration of 0.6 µM and with a 50 mM HEPES, pH 7.4, 50 mM NaCl buffer at RT. The λ max is the maximum fluorescence emission wavelength, $\langle\lambda\rangle$ is the fluorescence spectral center-of-mass, $\langle\tau\rangle$ is the amplitude-weighted mean fluorescence lifetime, and finally $\langle r\rangle$ is the steady-state fluorescence anisotropy. Results for A2C-Acrylodan construct with LUVs 25:75 POPC:POPS were obtained by Dr. Tânia Sousa and are shown here to just compare with the results from this thesis.

Construct	Medium	λ max (nm)	$\langle\lambda\rangle$ (nm)	$\langle r\rangle$	$\langle\tau\rangle$ (ns)
Httex1-23Q-A2C	**Buffer**	524	527	0.12	0.95
	POPC	498	503	0.16	2.04
	1:1:1 SM:Chol:POPC	493	500	0.15	1.60
	25:75 POPS:POPS	471	486	0.18	2.63
Httex1-23Q-A82C	**Buffer**	532	543	0.12	1.31
	POPC	530	533	0.11	1.44
	1:1:1 SM:Chol:POPC	529	536	0.11	1.41
	25:75 POPC:POPS	531	528	0.12	1.50

3.2.2 Characterization of the Nt17 domain (Httex1-23Q-A2C-Acrylodan) in the presence of lipid vesicles

Previous studies show that the Nt17 domain of Httex1 interacts with lipid membranes [87]. Moreover, it was stated that when this domain is in solution (not bound to lipids), it does not adopt a stable secondary structure. It is only when binding with lipid membranes that this domain structure is stabilized [43]. It is also assumed that this binding allows for the formation of a stable α-helical conformation within the Nt17 domain.

The Httex1-23Q-A2C-Acrylodan construct was used here to map changes in the local polarity within the Nt17 domain upon membrane interaction. It is expected that when Acrylodan shifts from an environment with high polarity (solution) to a more hydrophobic environment (such as lipid membranes), the maximum emission wavelength will shift towards lower wavelengths. That is often referenced as a blue shift.

The interaction of Httex1-23Q-A2C-Acrylodan with fluid/zwitterionic lipid membranes composed of pure POPC was initially characterized. Upon increasing the lipid concentration, the Acrylodan fluorescence intensity and the mean fluorescence lifetime increased. At 1 mM of POPC LUVs (Table 3.1), there are noticeable differences in the fluorescent properties observed for the A2C construct (λ max = 498 nm, $\langle\lambda\rangle$ = 503 nm, $\langle r\rangle$ = 0.16, $\langle\tau\rangle$ = 2.04 ns) when compared to the solution state (in buffer). The blue-shift (Figure 3.4(A)) in both λ max and $\langle\lambda\rangle$ (-26 nm and -24 nm, respectively) indicate that Acrylodan is present in a less polar environment upon adding POPC vesicles. The values are somewhat consistent (at lower extents) to previous findings that showed similar results when a protein labeled with Acrylodan is embedded in a lipid layer [86]. In addition, the increase in the steady-state fluorescence anisotropy suggests that the fluorescent probe (in the A2C position) is more constrained (a lower "freedom of movement"), reporting the membrane-binding.

The binding of Httex1-23Q-A2C-Acrylodan with 1:1:1 SM:Chol:POPC LUVs with co-existing of liquid ordered (lo) or disordered (ld) phases was also studied. The results (Table 3.1 and Figure 3.4(C)) obtained for this ternary lipid mixture (λ max = 493 nm, $\langle\lambda\rangle$ = 500 nm, $\langle r\rangle$ = 0.15, $\langle\tau\rangle$ = 1.60 ns) were very similar to the ones obtained for pure POPC vesicles. This supports that Nt17 domain also interfaces the lipid vesicles.

The interaction of Httex1-23Q-A2C-Acrylodan with lipid vesicles containing 25:75 POPC:POPS (negatively-charged membranes) was not performed during this work, as the results were previously obtained in the host lab by Dr. Tânia Sousa. Therefore, the fluorescence emission spectra are not presented in Figure 3.3, but the properties observed are available for comparison with the other lipid mixtures used in Figure 3.4, Figure 3.5 and Table 3.1. The results obtained with 25:75 POPC:POPS LUVs show that the Httex1-23Q interaction with anionic lipid membranes was of a greater extent when compared to POPC and 1:1:1 SM:Chol:POPC lipid vesicles.

Overall, the results indicate that the binding of Httex1-23Q to lipid membranes is primarily driven by an electrostatic component, shown by the preference for the negatively-charged POPS lipid vesicles. However, data obtained for other lipid mixtures show that there is also a hydrophobic factor present in this interaction. In addition, the results are also consistent with previous studies reporting that Nt17 domain plays a direct role in the Httex1-membrane binding.

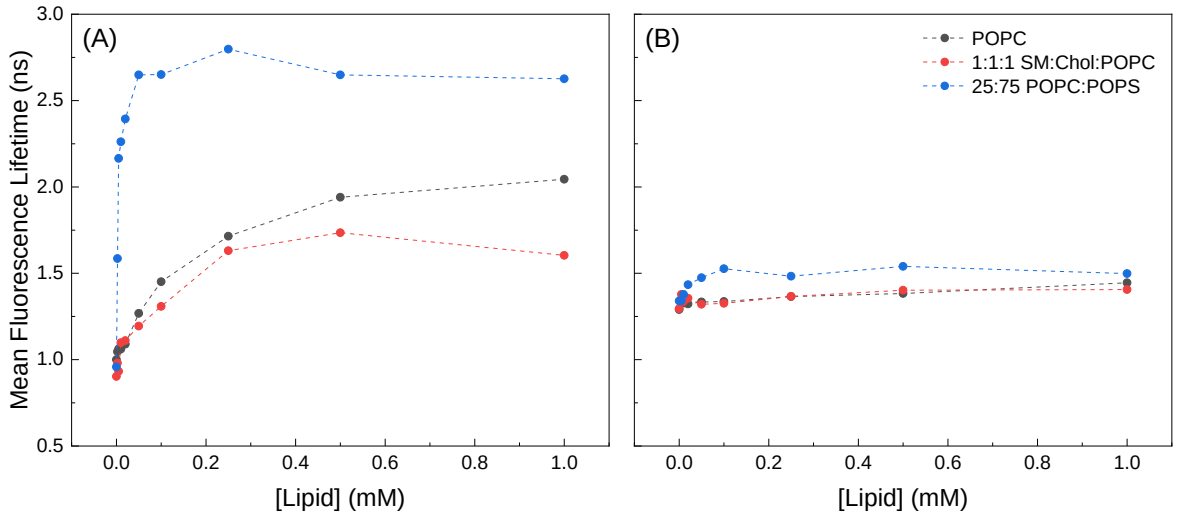

Figure 3.5 – Changes in the amplitude-weighted mean fluorescence lifetime ($\langle\tau\rangle$) of (A) Httex1-23Q-A2C-Acrylodan and (B) Httex1-23Q-A82C-Acrylodan with increasing lipid concentrations. The measurements were performed with LUVs composed of pure POPC (black); 1:1:1 SM:Chol:POPC (red); and 25:75 POPC:POPS (blue). Dashed lines were drawn as guides to the eye. The samples had a protein concentration of 0.6 µM and were in a 50 mM HEPES, pH 7.4, 50 mM NaCl buffer at RT. Results obtained for Httex1-23Q-A2C-Acrylodan with 25:75 POPC:POPS LUVs were acquired by Dr. Tânia Sousa and are shown here to just compare with the results from this work.

3.2.3 Characterization of the PRR (Httex1-23Q-A82C-Acrylodan) in the presence of lipid vesicles

Previous studies show that the PRR does not adopt a stable secondary/tertiary structure and it is an IDP in solution [88]. In this work, the Httex1-23Q-A82C construct was used to investigate the PRR region's behavior under different lipid mixtures and concentrations (Figure 3.4 and Figure 3.5).

Upon increasing the lipid concentration and for all three lipid mixtures, the magnitude of changes in the fluorescence properties of Httex1-23Q-A82C-Acrylodan were significantly smaller than the obtained for the Httex1-23Q-A2C-Acrylodan. There was only a very slight blue-shift in $\langle\lambda\rangle$ and λ max (even for LUVs containing 25:75 POPC:POPS lipid mixture). Moreover, both the steady-state anisotropy and the mean fluorescence lifetime remained practically unchanged.

Altogether, these results show that PRR remains exposed to the solvent Httex1-23Q is in the membrane-bound state, and in contrast the Nt17 domain is directly involved in the membrane-binding of Httex1-23Q (section 3.2.2).

3.3 Time-resolved fluorescence anisotropy measurements of Httex1-23Q-A2C and -A82C-Atto488

Atto 488 maleimide is also a thiol reactive probe and has a higher absorption coefficient, quantum yield, photo-stability, and fluorescence lifetime than Acrylodan [68]. Atto 488 was chosen to probe the conformational dynamics at both termini using the same labeling positions (A2C – Nt17 or A82C – PRR). Specifically, time-resolved fluorescence anisotropy experiments were performed with Httex1-23Q-A2C-Atto488 and Httex1-23Q-A82C-Atto488 free in solution (buffer) and with 1 mM LUVs (fully bound). Again, LUVs were prepared with pure POPC, 1:1:1 SM:Chol:POPC and 25:75 POPC:POPS.

The anisotropy decays were fitted by a sum of two exponentials terms: ϕ_1 represents the depolarization of the fluorescent probe; and ϕ_2 denotes the depolarization of the polypeptide chain of the Httex1-23Q protein. The results obtained from the anisotropy decays analysis of both Httex1-23Q-A2C and -A82C-Atto488 constructs are summarized in Table 3.2.

Table 3.2 – Time-resolved fluorescence anisotropy parameters of Httex1-23Q-A2C-Atto488 and Httex1-23Q-A82C-Atto488 in buffer (solution) and with 1 mM LUVs (POPC, 1:1:1 SM:Chol:POPC and 25:75 POPC:POPS). β_i is the normalized amplitudes and ϕ_i is the rotational correlation times. $\langle r \rangle_{exp}$) is the steady-state fluorescence anisotropy; and finally, $\langle r \rangle_{calc}$ is the anisotropy calculated from the parameters of the time-resolved analyses.

Construct	Solution	$r(0)$	β_1	ϕ_1 (ns)	β_2	ϕ_2 (ns)	X^2	$\langle r \rangle_{exp}$	$\langle r \rangle_{calc}$
Httex1-23Q-A2C	Buffer	0.335	0.235	0.335	0.100	2.506	1.123	0.074	0.069
	POPC	0.395	0.225	0.185	0.170	1.275	1.274	0.076	0.069
	1:1:1 SM:Chol:POPC	0.394	0.277	0.248	0.117	3.022	1.458	0.077	0.080
	25:75 POPC:POPS	0.403	0.299	0.331	0.104	7.964	1.252	0.103	0.090
Httex1-23Q-A82C	Buffer	0.390	0.242	0.175	0.148	1.688	1.185	0.057	0.052
	POPC	0.397	0.241	0.208	0.156	1.271	1.402	0.064	0.059
	1:1:1 SM:Chol:POPC	0.396	0.240	0.197	0.156	1.471	1.551	0.067	0.064
	25:75 POPC:POPS	0.388	0.218	0.176	0.170	0.887	1.205	0.056	0.056

In solution (buffer), the anisotropy decays of both Httex1-23Q-A2C-Atto488 and -A82C-Atto488 were similar, and they are characterized by a high β_1 amplitude (for ϕ_1), reflecting a high contribution of the fast rotation of the fluorophore (Atto 488) that is typical of IDPs.

In the presence of lipid membranes, the anisotropy decays of Httex1-23Q-A2C-Atto488 only experienced major changes upon interaction with anionic vesicles (25:75 POPC:POPS). Specifically, the second rotational correlation time increased for ϕ_2 = 7.96, reflecting that the Nt17 (A2C-postion) interfaces the lipid membranes and adopts a less flexible state. For the Httex1-23Q-A82C-Atto488, we did not detect significant variations in the anisotropy decays upon adding 1mM LUVs and for all lipid compositions. This is consistent with our Acrylodan data that the PRR of Httex1 is not involved in the membrane interaction, remining highly flexible/dynamic in the membrane-bound state.

Overall, these data show that N17 adopts a less flexible state upon binding to negatively-charged membranes. The PRR remains highly dynamic even upon membrane binding (independently of the lipid composition).

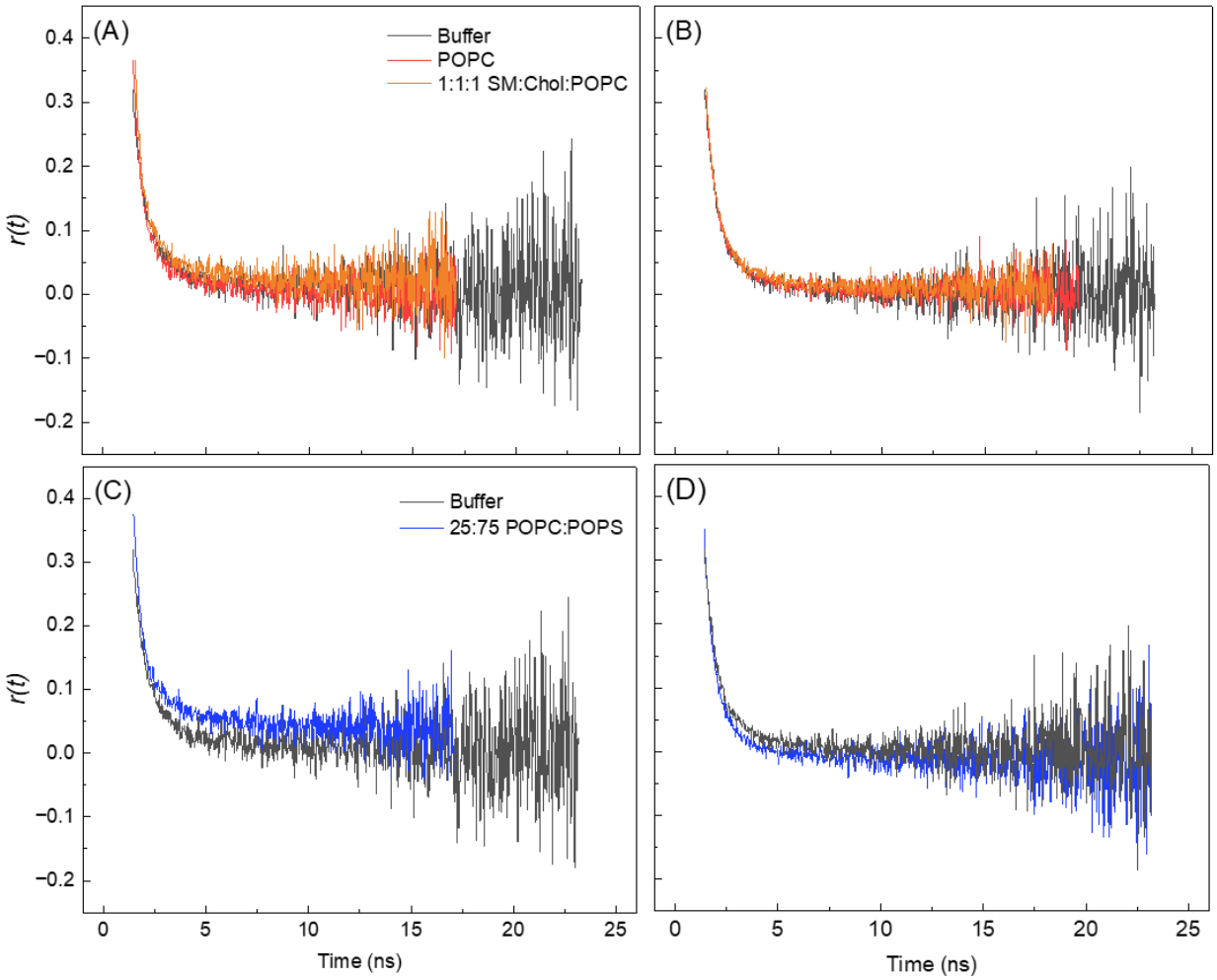

Figure 3.6 – Time-resolved fluorescence anisotropy decays of (A-C) Httex1-23Q-A2C-Atto488 and (B-D) Httex1-23Q-A82C-Atto488 in buffer (grey), and in the presence of 1 mM LUVs of POPC (red), 1:1:1 SM:Chol:POPC (orange) and 25:75 POPC:POPS (blue).

3.4 Calibration of the smFRET setup and characterization of the double-labeled Httex1-23Q

System calibrations were performed to optimize the optical pathway and setup. First, by using 10nM of Rhodamine 110 in water, the optimal Z-position of the optical fibers was determined. Specifically, several FCS measurements (10 curves for 10 seconds each) were conducted at different Z-positions, with the objective of obtaining the best counts per molecule (cpm) and diffusion time (τ_D) for each channel (Figure 3.7). These parameters should be consistent from day to day, for a given laser power.

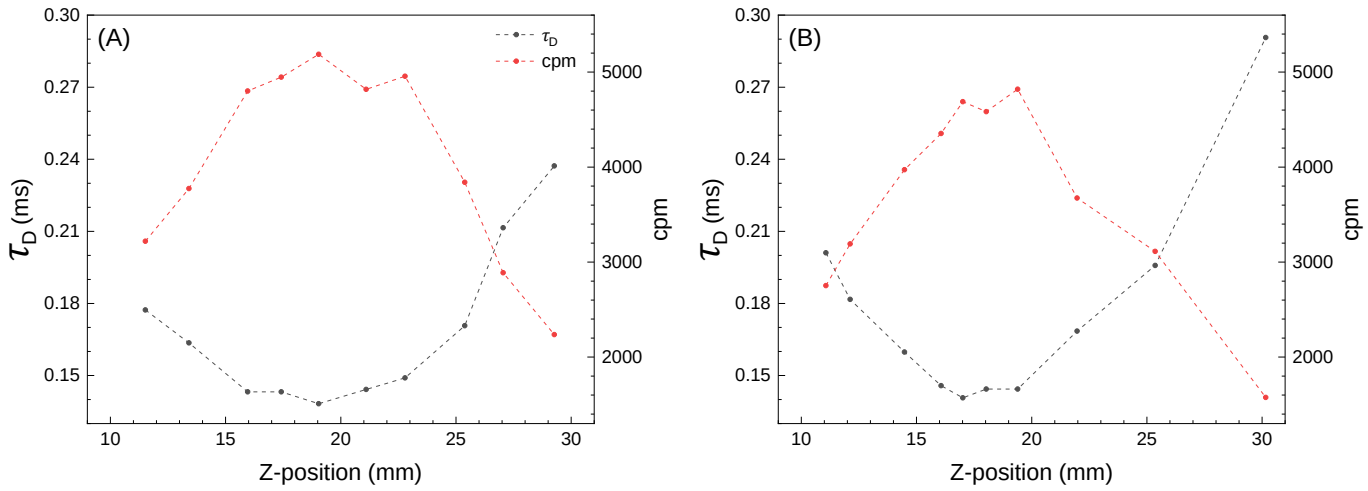

Figure 3.7 – Calibration of the Z-position of the (A) donor and (B) acceptor optical fibers. The variation of the diffusion time (τ_D) – in grey – and the counts per molecule (cpm) – red – with the Z-position was determined by FCS. The dashed lines serve as guides to the eye.

Secondly, we determined the confocal volume (*s*-factor) and bleed-through of the donor fluorescence into the acceptor channel (β-factor) by FCS measurements of 10 nM Alexa 488 in water. The FCS curves were analyzed by Equation 9 to determine the *s*-factor. At the same time, the intensities in both channels were recorded and the β-factor was calculated by the ratio of intensities measured in the acceptor channel regarding the donor channel.

Thirdly, we used the 10-mer dsDNA (with the donor/acceptor pair) as a positive FRET standard control. 10-minute measurements were performed, and the FRET histograms were fitted with multipeak Gaussian functions. The ET_{eff} determined for the double-labelled DNA is similar to the expected value.

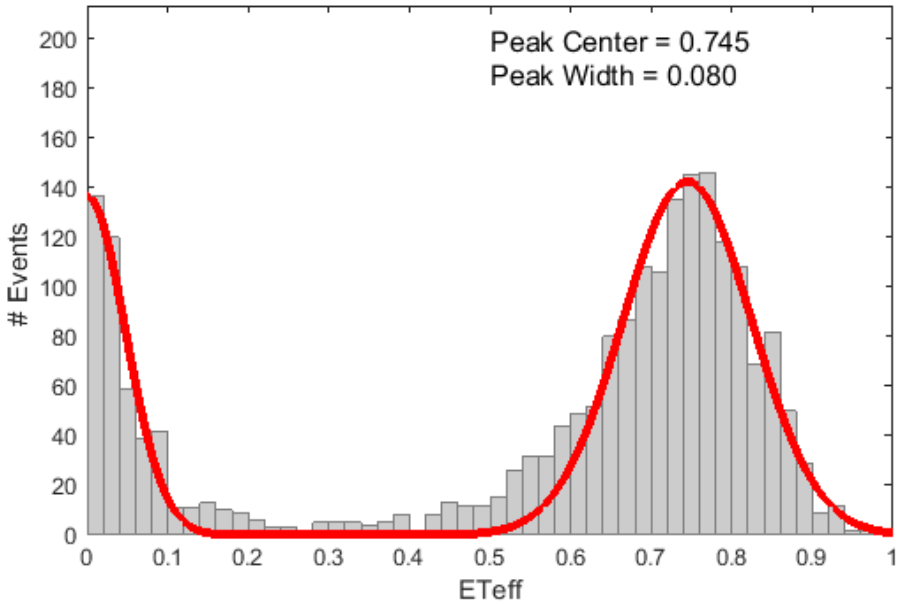

Figure 3.8 – smFRET calibration with 10-mer dsDNA. A measurement of 10 minutes was performed to determine the ET_{eff} for the 10-mer dsDNA. The smFRET histogram was fitted with a two-gaussian distribution.

The double-labeled Httex1-23Q-A2C/A82C protein (with Alexa 488 and 594 maleimide) was also characterized by smFRET. Unfortunately, the result (Figure 3.9) show that the labeling was not efficient and there was only donor-labeled protein (without donor/acceptor pairs). Furthermore, our samples also had significant background and also absorption to the glass coverslip [64]. In the future, a new double-labeling of the Httex1-23Q protein should be carried out and troubleshoot the background of each buffer component (including using water of spectroscopic grade).

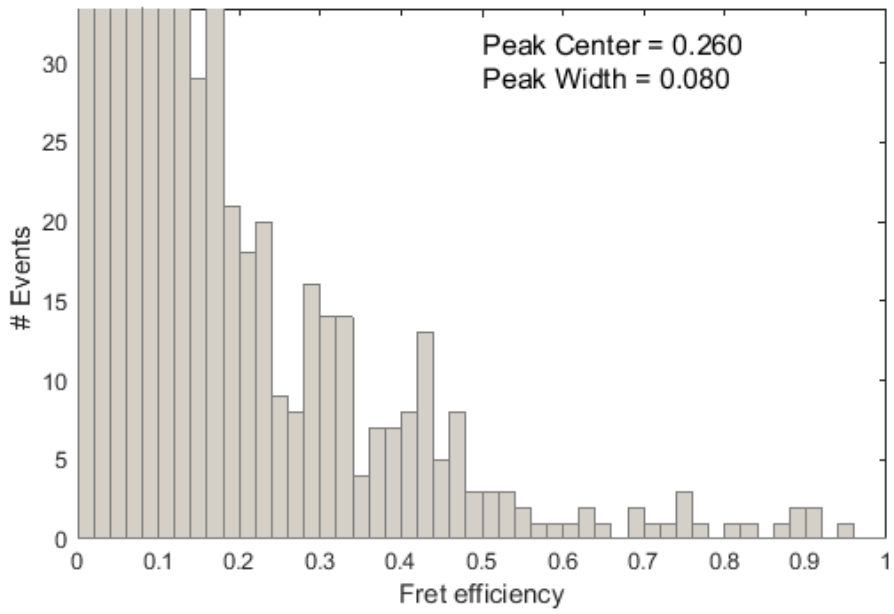

Figure 3.9 – Characterization of the double-labeled Httex1-23Q-A2C/A82C protein by smFRET.

4 Conclusion and final remarks

HD is a fatal and inherited progressive neurodegenerative disease caused by an expansion of the polyQ domain at the first exon of the HTT protein (Httex1). Growing evidence supports that lipid membranes are critical in the mechanism of Httex1 neurotoxicity. However, so far most biophysical studies have focused on using synthetic polyQ peptides to evaluate membrane interaction. However, recent works support that both flanking polyQ regions – Nt17 and PRR – modulate the Httex1 aggregation in solution and in the presence of lipid membranes [34], [52], [54].

This work aimed to evaluate the interaction of Httex1-23Q (WT variant – full-length fragment) with lipid vesicles of variable composition: (1) fluid/zwitterionic pure POPC; (2) 1:1:1 SM:Chol:POPC with co-existing of liquid ordered (lo) or disordered (ld) phases; and finally (3) 25:75 POPC:POPS for probe electrostatic effects. Httex1-23Q was engineered to introduce a single-cysteine at position A2C or A82C (probing Nt17 and PRR, respectively) for labelling with Acrylodan and Atto 488 maleimide; or introduce two-cysteines (A2C and A82C) for double-labelling with Alexa 488 and 584 maleimide for smFRET measurements.

The Httex1-lipid interaction was initially characterized by Acrylodan fluorescence (steady-state and time-resolved measurements). Here, Acrylodan was used to probe changes in the local polarity and consequently evaluate membrane-binding. Our data shows that Httex1-23Q-A2C-Acrylodan binds to LUVs composed of SM:Chol:POPC and pure POPC vesicles, revealing there is a hydrophobic component in this interaction and no preference for ordered phase. However, this interaction was lower than for POPS-containing vesicles (data obtained previously by Dr. Tânia Sousa). Moreover, the data obtained for Httex1-23Q-A82C-Acrylodan indicate that the C-terminal PRR is completely solvent exposed in the Httex1-23Q membrane-bound state.

At second phase, the conformational dynamics of both Nt17 and PRR upon membrane binding was evaluated through time-resolved fluorescence anisotropy measurements. Here, Httex1-23Q-A2C and -A82C was labelled with Atto 488 maleimide, and their anisotropy decays were recorded in solution and in the presence of 1mM LUVs. Altogether, these data reveal that Nt17 interfaces POPS-containing vesicles and adopts a less flexible state. While PRR keep its solution conformational dynamics (for all distinct lipid compositions).

These results are consistent with previous studies showing that Nt17 anchors to lipid membranes and forms an amphipathic a-helix [43]. Moreover, a previous AFM study of K. A. Burke, *et al.* [34] also revealed that PRR alone was not sufficient to induce polyQ interaction with a lipid surface.

Finally, we also attempted to map the global dimensions of Httex1-23Q in the membrane-bound state. In the context of this thesis, the smFRET setup was calibrated (Z-position of the optical fibers and also determine the ET_{eff} of a positive control 10-mer dsDNA). The Httex1-23Q-A2C/A82C was double-labeled with Atto488 and 594 maleimide and further characterized by smFRET. Our smFRET data indicates that the labeling was not efficient and only resulted in donor-only labeled Httex1-23Q. Further studies should focus on optimizing the double-labeling protocol for Httex1-23Q. Moreover, the creation of more smFRET constructs will allow to also determine conformational assemble of Httex1-23Q at the membrane surface.

References

[1] S. N. Illarioshkin, S. A. Klyushnikov, V. A. Vigont, Yu. A. Seliverstov, and E. V. Kaznacheyeva, 'Molecular Pathogenesis in Huntington's Disease', *Biochem. Mosc.*, vol. 83, no. 9, pp. 1030–1039, Sep. 2018.

[2] M. E. MacDonald *et al.*, 'A novel gene containing a trinucleotide repeat that is expanded and unstable on Huntington's disease chromosomes', *Cell*, vol. 72, no. 6, pp. 971–983, Mar. 1993.

[3] S. S. Baig, M. Strong, and O. W. Quarrell, 'The global prevalence of Huntington's disease: a systematic review and discussion', *Neurodegener. Dis. Manag.*, vol. 6, no. 4, pp. 331–343, Aug. 2016.

[4] P. Dayalu and R. L. Albin, 'Huntington Disease', *Neurol. Clin.*, vol. 33, no. 1, pp. 101–114, Feb. 2015.

[5] Nicholas S Caron, G. E. Wright, and M. R. Hayden, 'Huntington Disease', *Huntingt. Dis.*, p. 34.

[6] F. Squitieri, L. Frati, A. Ciarmiello, S. Lastoria, and O. Quarrell, 'Juvenile Huntington's disease: Does a dosage-effect pathogenic mechanism differ from the classical adult disease?', *Mech. Ageing Dev.*, vol. 127, no. 2, pp. 208–212, Feb. 2006.

[7] T. C. Vale and F. Cardoso, 'Chorea: A Journey through History', *Tremor Hyperkinetic Mov.*, vol. 5, no. 0, Art. no. 0, May 2015.

[8] G. Huntington, 'On Chorea', *Med. Surg. Report. Wkly. J.*, vol. 26, no. 15, pp. 317–321, Apr. 1872.

[9] 'Chorea Information Page | National Institute of Neurological Disorders and Stroke'. https://www.ninds.nih.gov/Disorders/All-Disorders/Chorea-Information-Page (accessed Feb. 03, 2022).

[10] P. McColgan and S. J. Tabrizi, 'Huntington's disease: a clinical review', p. 11, 2017.

[11] G. Bates, P. S. Harper, and L. Jones, Eds., *Huntington's disease*, 3rd ed. in Oxford monographs on medical genetics, no. no. 45. Oxford ; New York: Oxford University Press, 2002.

[12] F. O. Walker, 'Huntington's disease', *The Lancet*, vol. 369, no. 9557, pp. 218–228, Jan. 2007.

[13] PubChem, 'HTT - huntingtin (human)'. https://pubchem.ncbi.nlm.nih.gov/gene/HTT/human (accessed Feb. 02, 2022).

[14] J. A. Sayer, M. Manczak, L. Akileswaran, P. H. Reddy, and V. M. Coghlan, 'Interaction of the nuclear matrix protein NAKAP with HypA and huntingtin', *NeuroMolecular Med.*, vol. 7, no. 4, pp. 297–310, Nov. 2005.

[15] F. Saudou and S. Humbert, 'The Biology of Huntingtin', *Neuron*, vol. 89, no. 5, pp. 910–926, Mar. 2016.

[16] M. P. Duyao *et al.*, 'Inactivation of the mouse Huntington's disease gene homolog Hdh', *Science*, vol. 269, no. 5222, pp. 407–410, Jul. 1995.

[17] W. Auerbach, 'The HD mutation causes progressive lethal neurological disease in mice expressing reduced levels of huntingtin', *Hum. Mol. Genet.*, vol. 10, no. 22, pp. 2515–2523, Oct. 2001.

[18] J. M. M. B. dos Santos, 'The Role of Post-Translational Modifications on the Oligomerization, Aggregation and Toxicity of Mutant Huntingtin', PhD Thesis, Faculdade de Medicina da Universidade Lisboa, 2018.

[19] F. G. Gervais *et al.*, 'Recruitment and activation of caspase-8 by the Huntingtin-interacting protein Hip-1 and a novel partner Hippi', *Nat. Cell Biol.*, vol. 4, no. 2, pp. 95–105, Feb. 2002.

[20] J. R. Arndt, M. Chaibva, and J. Legleiter, 'The emerging role of the first 17 amino acids of huntingtin in Huntington's disease', *Biomol. Concepts*, vol. 6, no. 1, pp. 33–46, Mar. 2015.

[21] M. P. Parsons and L. A. Raymond, 'Chapter 20 - Huntington Disease', in *Neurobiology of Brain Disorders*, M. J. Zigmond, L. P. Rowland, and J. T. Coyle, Eds., San Diego: Academic Press, 2015, pp. 303–320.

[22] M. Tartari *et al.*, 'Phylogenetic Comparison of Huntingtin Homologues Reveals the Appearance of a Primitive polyQ in Sea Urchin', *Mol. Biol. Evol.*, vol. 25, no. 2, pp. 330–338, fevereiro 2008.

[23] P. Harjes and E. E. Wanker, 'The hunt for huntingtin function: interaction partners tell many different stories', *Trends Biochem. Sci.*, vol. 28, no. 8, pp. 425–433, Aug. 2003.

[24] M. Neveklovska, E. B. D. Clabough, J. S. Steffan, and S. O. Zeitlin, 'Deletion of the Huntingtin Proline-Rich Region does not Significantly Affect Normal Huntingtin Function in Mice', *J. Huntingt. Dis.*, vol. 1, no. 1, pp. 71–87, Jan. 2012.

[25] Y. J. Kim *et al.*, 'Caspase 3-cleaved N-terminal fragments of wild-type and mutant huntingtin are present in normal and Huntington's disease brains, associate with membranes, and undergo calpain-dependent proteolysis', *Proc. Natl. Acad. Sci. U. S. A.*, vol. 98, no. 22, pp. 12784–12789, Oct. 2001.

[26] A. Lunkes *et al.*, 'Proteases acting on mutant huntingtin generate cleaved products that differentially build up cytoplasmic and nuclear inclusions', *Mol. Cell*, vol. 10, no. 2, pp. 259–269, Aug. 2002.

[27] Q. Guo *et al.*, 'The cryo-electron microscopy structure of huntingtin', *Nature*, vol. 555, no. 7694, pp. 117–120, Mar. 2018.
[28] B. Huang *et al.*, 'HAP40 protein levels are huntingtin-dependent and decrease in Huntington disease', *Neurobiol. Dis.*, vol. 158, p. 105476, Oct. 2021.
[29] C. Landles and G. P. Bates, 'Huntingtin and the molecular pathogenesis of Huntington's disease', *EMBO Rep.*, vol. 5, no. 10, pp. 958–963, outubro 2004.
[30] K. Omi, N. S. Hachiya, M. Tanaka, K. Tokunaga, and K. Kaneko, '14-3-3zeta is indispensable for aggregate formation of polyglutamine-expanded huntingtin protein', *Neurosci. Lett.*, vol. 431, no. 1, pp. 45–50, Jan. 2008.
[31] G. P. Bates *et al.*, 'Huntington disease', *Nat. Rev. Dis. Primer*, vol. 1, no. 1, Art. no. 1, Apr. 2015.
[32] A. Adegbuyiro, F. Sedighi, A. W. Pilkington, S. Groover, and J. Legleiter, 'Proteins Containing Expanded Polyglutamine Tracts and Neurodegenerative Disease', *Biochemistry*, vol. 56, no. 9, pp. 1199–1217, Mar. 2017.
[33] M. Jayaraman *et al.*, 'Slow amyloid nucleation via α-helix-rich oligomeric intermediates in short polyglutamine-containing huntingtin fragments', *J. Mol. Biol.*, vol. 415, no. 5, pp. 881–899, Feb. 2012.
[34] K. A. Burke, K. J. Kauffman, C. S. Umbaugh, S. L. Frey, and J. Legleiter, 'The Interaction of Polyglutamine Peptides with Lipid Membranes Is Regulated by Flanking Sequences Associated with Huntingtin', *J. Biol. Chem.*, vol. 288, no. 21, pp. 14993–15005, May 2013.
[35] M. W. Kim, Y. Chelliah, S. W. Kim, Z. Otwinowski, and I. Bezprozvanny, 'Secondary Structure of Huntingtin Amino-Terminal Region', *Structure*, vol. 17, no. 9, pp. 1205–1212, setembro 2009.
[36] S. W. Davies *et al.*, 'Formation of neuronal intranuclear inclusions underlies the neurological dysfunction in mice transgenic for the HD mutation', *Cell*, vol. 90, no. 3, pp. 537–548, Aug. 1997.
[37] K. A. Burke, K. M. Hensal, C. S. Umbaugh, M. Chaibva, and J. Legleiter, 'Huntingtin disrupts lipid bilayers in a polyQ-length dependent manner', *Biochim. Biophys. Acta BBA - Biomembr.*, vol. 1828, no. 8, pp. 1953–1961, Aug. 2013.
[38] M. Arrasate, S. Mitra, E. S. Schweitzer, M. R. Segal, and S. Finkbeiner, 'Inclusion body formation reduces levels of mutant huntingtin and the risk of neuronal death', *Nature*, vol. 431, no. 7010, pp. 805–810, Oct. 2004.
[39] P. J. Muchowski, 'Protein misfolding, amyloid formation, and neurodegeneration: a critical role for molecular chaperones?', *Neuron*, vol. 35, no. 1, pp. 9–12, Jul. 2002.
[40] E. Lévy *et al.*, 'Causative Links between Protein Aggregation and Oxidative Stress: A Review', *Int. J. Mol. Sci.*, vol. 20, no. 16, Art. no. 16, Jan. 2019.
[41] J. D. Godin *et al.*, 'Huntingtin is required for mitotic spindle orientation and mammalian neurogenesis', *Neuron*, vol. 67, no. 3, pp. 392–406, Aug. 2010.
[42] L. R. Gauthier *et al.*, 'Huntingtin controls neurotrophic support and survival of neurons by enhancing BDNF vesicular transport along microtubules', *Cell*, vol. 118, no. 1, pp. 127–138, Jul. 2004.
[43] R. S. Atwal, J. Xia, D. Pinchev, J. Taylor, R. M. Epand, and R. Truant, 'Huntingtin has a membrane association signal that can modulate huntingtin aggregation, nuclear entry and toxicity', *Hum. Mol. Genet.*, vol. 16, no. 21, pp. 2600–2615, Nov. 2007.
[44] R. S. Atwal and R. Truant, 'A stress sensitive ER membrane-association domain in Huntingtin protein defines a potential role for Huntingtin in the regulation of autophagy', *Autophagy*, vol. 4, no. 1, pp. 91–93, Jan. 2008.
[45] M. DiFiglia *et al.*, 'Huntingtin is a cytoplasmic protein associated with vesicles in human and rat brain neurons', *Neuron*, vol. 14, no. 5, pp. 1075–1081, May 1995.
[46] A. Di Pardo *et al.*, 'Ganglioside GM1 induces phosphorylation of mutant huntingtin and restores normal motor behavior in Huntington disease mice', *Proc. Natl. Acad. Sci. U. S. A.*, vol. 109, no. 9, pp. 3528–3533, Feb. 2012.
[47] R. S. Atwal *et al.*, 'Kinase inhibitors modulate huntingtin cell localization and toxicity', *Nat. Chem. Biol.*, vol. 7, no. 7, pp. 453–460, Jul. 2011.
[48] X. Gu *et al.*, 'Serines 13 and 16 are critical determinants of full-length human mutant huntingtin induced disease pathogenesis in HD mice', *Neuron*, vol. 64, no. 6, pp. 828–840, Dec. 2009.
[49] J. S. Steffan *et al.*, 'SUMO modification of Huntingtin and Huntington's disease pathology', *Science*, vol. 304, no. 5667, pp. 100–104, Apr. 2004.
[50] K. A. Burke, E. A. Yates, and J. Legleiter, 'Biophysical Insights into How Surfaces, Including Lipid Membranes, Modulate Protein Aggregation Related to Neurodegeneration', *Front. Neurol.*, vol. 4, 2013.
[51] S. Subramaniam, K. M. Sixt, R. Barrow, and S. H. Snyder, 'Rhes, a striatal specific protein, mediates mutant-huntingtin cytotoxicity', *Science*, vol. 324, no. 5932, pp. 1327–1330, Jun. 2009.
[52] A. Bhattacharyya *et al.*, 'Oligoproline effects on polyglutamine conformation and aggregation', *J. Mol. Biol.*, vol. 355, no. 3, pp. 524–535, Jan. 2006.

[53] E. Rockabrand *et al.*, 'The first 17 amino acids of Huntingtin modulate its sub-cellular localization, aggregation and effects on calcium homeostasis', *Hum. Mol. Genet.*, vol. 16, no. 1, pp. 61–77, Jan. 2007.
[54] K. Shen *et al.*, 'Control of the structural landscape and neuronal proteotoxicity of mutant Huntingtin by domains flanking the polyQ tract', *eLife*, vol. 5, p. e18065, outubro 2016.
[55] P. A. Janmey and D. A. Weitz, 'Dealing with mechanics: mechanisms of force transduction in cells', *Trends Biochem. Sci.*, vol. 29, no. 7, pp. 364–370, Jul. 2004.
[56] V. Vogel and M. Sheetz, 'Local force and geometry sensing regulate cell functions', *Nat. Rev. Mol. Cell Biol.*, vol. 7, no. 4, Art. no. 4, Apr. 2006.
[57] M. Tao, N. K. Pandey, R. Barnes, S. Han, and R. Langen, 'Structure of Membrane-Bound Huntingtin Exon 1 Reveals Membrane Interaction and Aggregation Mechanisms', *Structure*, vol. 27, no. 10, pp. 1570-1580.e4, Oct. 2019.
[58] K. B. Kegel-Gleason, 'Huntingtin interactions with membrane phospholipids: strategic targets for therapeutic intervention?', *J. Huntingt. Dis.*, vol. 2, no. 3, pp. 239–250, 2013.
[59] S. Vieweg, A. Ansaloni, Z.-M. Wang, J. B. Warner, and H. A. Lashuel, 'An Intein-based Strategy for the Production of Tag-free Huntingtin Exon 1 Proteins Enables New Insights into the Polyglutamine Dependence of Httex1 Aggregation and Fibril Formation', *J. Biol. Chem.*, vol. 291, no. 23, pp. 12074–12086, Jun. 2016.
[60] C. W. F. McClare, 'An accurate and convenient organic phosphorus assay', *Anal. Biochem.*, vol. 39, no. 2, pp. 527–530, Feb. 1971.
[61] 'Avanti Polar Lipids, Inc. | Smarter Innovation Through Quality', *Avanti Polar Lipids*. https://avantilipids.com/ (accessed Oct. 24, 2022).
[62] 'Life Technologies - PT'. https://www.thermofisher.com/uk/en/home.html (accessed Feb. 23, 2023).
[63] X.-H. Li, J. A. Culver, and E. Rhoades, 'Tau Binds to Multiple Tubulin Dimers with Helical Structure', *J. Am. Chem. Soc.*, vol. 137, no. 29, pp. 9218–9221, Jul. 2015.
[64] A. M. Melo, S. Elbaum-Garfinkle, and E. Rhoades, 'Insights into tau function and dysfunction through single-molecule fluorescence', *Methods Cell Biol.*, vol. 141, pp. 27–44, 2017.
[65] A. M. Melo, J. Coraor, G. Alpha-Cobb, S. Elbaum-Garfinkle, A. Nath, and E. Rhoades, 'A functional role for intrinsic disorder in the tau-tubulin complex', *Proc. Natl. Acad. Sci. U. S. A.*, vol. 113, no. 50, pp. 14336–14341, Dec. 2016.
[66] A. Froger and J. E. Hall, 'Transformation of plasmid DNA into *E. coli* using the heat shock method', *J. Vis. Exp. JoVE*, no. 6, p. 253, 2007.
[67] F. G. Prendergast, M. Meyer, G. L. Carlson, S. Iida, and J. D. Potter, 'Synthesis, spectral properties, and use of 6-acryloyl-2-dimethylaminonaphthalene (Acrylodan). A thiol-selective, polarity-sensitive fluorescent probe', *J. Biol. Chem.*, vol. 258, no. 12, pp. 7541–7544, Jun. 1983.
[68] 'ATTO 488', *ATTO-TEC GmbH*. https://www.atto-tec.com/ATTO-488.html?language=en (accessed Oct. 05, 2022).
[69] 'Pierce™ Modified Lowry Protein Assay Kit'. https://www.thermofisher.com/order/catalog/product/23240 (accessed Feb. 03, 2022).
[70] 'Pierce™ BCA Protein Assay Kit'. https://www.thermofisher.com/order/catalog/product/23225 (accessed Sep. 05, 2022).
[71] R. F. M. de Almeida, A. Fedorov, and M. Prieto, 'Sphingomyelin/Phosphatidylcholine/Cholesterol Phase Diagram: Boundaries and Composition of Lipid Rafts', *Biophys. J.*, vol. 85, no. 4, pp. 2406–2416, Oct. 2003.
[72] D. H. J. Lopes, A. Chapeaurouge, G. A. Manderson, J. S. Johansson, and S. T. Ferreira, 'Redesigning the folding energetics of a model three-helix bundle protein by site-directed mutagenesis', *J. Biol. Chem.*, vol. 279, no. 12, pp. 10991–10996, Mar. 2004.
[73] G. Scanavachi, A. Coutinho, A. A. Fedorov, M. Prieto, A. M. Melo, and R. Itri, 'Lipid Hydroperoxide Compromises the Membrane Structure Organization and Softens Bending Rigidity', *Langmuir*, vol. 37, no. 33, pp. 9952–9963, Aug. 2021.
[74] A. M. Melo, J. C. Ricardo, A. Fedorov, M. Prieto, and A. Coutinho, 'Fluorescence Detection of Lipid-Induced Oligomeric Intermediates Involved in Lysozyme "Amyloid-Like" Fiber Formation Driven by Anionic Membranes', *J. Phys. Chem. B*, vol. 117, no. 10, pp. 2906–2917, Mar. 2013.
[75] A. M. Melo, A. Fedorov, M. Prieto, and A. Coutinho, 'Exploring homo-FRET to quantify the oligomer stoichiometry of membrane-bound proteins involved in a cooperative partition equilibrium', *Phys. Chem. Chem. Phys.*, vol. 16, no. 34, pp. 18105–18117, Aug. 2014.
[76] J. R. Lakowicz, *Principles of fluorescence spectroscopy*, 3rd ed. New York: Springer, 2006.
[77] R. Roy, S. Hohng, and T. Ha, 'A practical guide to single-molecule FRET', *Nat. Methods*, vol. 5, no. 6, pp. 507–516, Jun. 2008.

[78] L. C. Hwang, J. Hohlbein, S. J. Holden, and A. N. Kapanidis, ‘Single-Molecule FRET: Methods and Biological Applications’, in *Handbook of Single-Molecule Biophysics*, P. Hinterdorfer and A. Oijen, Eds., New York, NY: Springer US, 2009, pp. 129–163.
[79] A. J. Trexler and E. Rhoades, ‘Single Molecule Characterization of α-Synuclein in Aggregation-Prone States’, *Biophys. J.*, vol. 99, no. 9, pp. 3048–3055, Nov. 2010.
[80] A. C. M. Ferreon, Y. Gambin, E. A. Lemke, and A. A. Deniz, ‘Interplay of α-synuclein binding and conformational switching probed by single-molecule fluorescence’, *Proc. Natl. Acad. Sci. U. S. A.*, vol. 106, no. 14, pp. 5645–5650, Apr. 2009.
[81] A. Reif, A. Chiki, J. Ricci, and H. A. Lashuel, ‘Generation of Native, Untagged Huntingtin Exon1 Monomer and Fibrils Using a SUMO Fusion Strategy’, *J. Vis. Exp.*, no. 136, p. 57506, Jun. 2018.
[82] ‘Expasy - Compute pI/Mw tool’. https://web.expasy.org/compute_pi/ (accessed Mar. 27, 2023).
[83] R. E. Hibbs, T. T. Talley, and P. Taylor, ‘Acrylodan-conjugated Cysteine Side Chains Reveal Conformational State and Ligand Site Locations of the Acetylcholine-binding Protein’, *J. Biol. Chem.*, vol. 279, no. 27, pp. 28483–28491, Jul. 2004.
[84] R. Zhou, X. Lu, Q. Yang, and P. Wu, ‘Nanocrystals for large Stokes shift-based optosensing’, *Chin. Chem. Lett.*, vol. 30, no. 10, pp. 1843–1848, Oct. 2019.
[85] J. Kranz, F. AlAzzam, A. Saluja, J. Svitel, and W. Al-Azzam, ‘Techniques for Higher-Order Structure Determination’, in *Biophysics for Therapeutic Protein Development*, L. O. Narhi, Ed., in Biophysics for the Life Sciences. New York, NY: Springer, 2013, pp. 33–82.
[86] R. Krishnan and S. L. Lindquist, ‘Structural insights into a yeast prion illuminate nucleation and strain diversity’, *Nature*, vol. 435, no. 7043, pp. 765–772, Jun. 2005.
[87] S. Vieweg *et al.*, ‘The Nt17 Domain and its Helical Conformation Regulate the Aggregation, Cellular Properties and Neurotoxicity of Mutant Huntingtin Exon 1’, *J. Mol. Biol.*, vol. 433, no. 21, p. 167222, Oct. 2021.
[88] J. B. Warner, K. M. Ruff, P. S. Tan, E. A. Lemke, R. V. Pappu, and H. A. Lashuel, ‘Monomeric Huntingtin Exon 1 Has Similar Overall Structural Features for Wild-Type and Pathological Polyglutamine Lengths’, *J. Am. Chem. Soc.*, vol. 139, no. 41, pp. 14456–14469, Oct. 2017.